Statistical Analysis of Contrail to Cirrus Evolution during the Contrail and Cirrus Experiments (CONCERT)

Aurélien Chauvigné[1], Olivier Jourdan[1], Alfons Schwarzenboeck[1], Christophe Gourbeyre[1], Jean François Gayet[1], Christiane Voigt[2,3], Hans Schlager[2], Stefan Kaufmann[2], Stephan Borrmann[3,4], Sergej Molleker[3,4], Andreas Minikin[2.5], Tina Jurkat[2], Ulrich Schumann[2]

[1]Laboratoire de Météorologie Physique, UMR 6016 CNRS/Université Clermont Auvergne, Clermont-Ferrand, France.
[2]Institut für Physik der Atmosphäre, Deutsches Zentrum für Luft- und Raumfahrt (DLR), Oberpfaffenhofen, Germany.
[3]Institut für Physik der Atmosphäre, Universität Mainz, Mainz, Germany.
[4]Max-Planck-Institute for Chemistry, Department for Particle Chemistry, Mainz, Germany.
[5]Now at: Flugexperimente, Deutsches Zentrum für Luft- und Raumfahrt (DLR), Oberpfaffenhofen, Germany.

Abstract:

Air traffic affects cloudiness, and thus climate, by emitting exhaust gases and particles. The study of the evolution of contrail properties is very challenging due to the complex interplay of vortex dynamics and atmospheric environment (e.g. temperature, supersaturation). Despite substantial progress in recent years, the optical, microphysical, and macrophysical properties of contrails and ambient cirrus during contrail formation and subsequent ageing are still subject to large uncertainties due to instrumental and observational limitations and the large number of variables influencing the contrail life cycle. In this study, various contrail cases corresponding to different aircraft types and atmospheric conditions are investigated using a statistical method based on the in situ optical measurements performed during the CONCERT campaigns 2008 and 2011. The two aircraft campaigns encompass more than 17 aircraft contrail cases. A Principal Component Analysis (PCA) of the angular scattering coefficients measured by the Polar Nephelometer is implemented. The goal is to classify the sampled ice cloud measurements in several clusters representative of different contrail development stages (primary wake, young contrail, aged contrail, and cirrus). Extinction and asymmetry coefficients, nitrogen oxide concentrations, relative humidity with respect to ice and particle size distributions are analysed for each cluster to characterize the evolution of ice-cloud properties during the contrail to cirrus evolution. The PCA demonstrates that contrail optical properties are well suited to identify and discriminate the different contrail growth stages and to characterize the evolution of contrail properties.

1 Introduction

Aircraft exhaust plumes have a significant impact on climate and tropospheric chemistry (Lee et al., 2010; IPCC, 1999). The Intergovernmental Panel for Climate Change IPCC Special Report on Aviation (1999) estimates that NO_x emissions from subsonic aircraft increase ozone concentrations at cruise level. Short and long-lived pollution species have different impact on atmospheric chemical composition depending on the flight level (Frömming et al, 2012). Emissions of water vapour, black carbon (BC) / soot particles, sulphate (SO_4) aerosols and nitrogen oxides (NO_x) contribute to the modification of the chemical composition of the upper troposphere on shorter timescales (Lee et al., 2010, Gettelman and Chen, 2013; Liou et al., 2013). The long-term climate impact is mainly driven by CO_2 emissions. Modelling studies have shown that the direct radiative forcing from aviation is expected to represent 3-4% (50-60 mW m^{-2}) of the anthropogenic

forcing (Lee et al., 2010; De Leon et al., 2012) and could reach 87 mW m^{-2} in 2025 (Chen and Gettelman, 2016). Aircraft induced cloudiness has also an important impact on climate, although the quantitative assessment of the radiative forcing remains a major source of uncertainties (Lee et al., 2010).

1.1. Contrail formation and evolution

Contrail formation is mainly controlled by the thermodynamic properties of the ambient air and by the aircraft emissions. The conditions for contrail formation can be determined by the Schmidt-Appleman Criterion (SAC) (Schumann, 1996). Contrail chemical composition can have a significant impact on the contrail formation (Kärcher et al., 2009). Indeed, contrail microphysical properties such as the total number densities and ice crystal diameters are directly linked to the emission index (e.g. soot emission index in kg-fuel^{-1}). Several studies in the past have been dedicated to the evolution of concentrations of nitrogen oxide (NO) and sulphur dioxide (SO$_2$) and their oxidized forms (Kärcher and Voigt, 2006 ; Voigt et al., 2006 ; Schäuble et al., 2009 ; Jurkat et al., 2011).

Two different processes of contrail formation have been studied: combustion condensation trails and aerodynamic condensation trails. Different studies (Gierens and Dilger, 2013; Jansen and Heymsfield, 2015) have illustrated characteristics of aerodynamically controlled contrail formation associated to warmer temperatures (observations at temperatures above -38°C). Contrails primarily initiated by the combustion processes result from the mixing of hot and humid exhaust gases with cooler and dryer ambient air. This increases the local relative humidity in the exhaust plume leading to the formation of contrails when the saturation with respect to liquid water is reached. In this case, soot and sulphate aerosols emitted by the aircraft (Moore et al., 2017) may act as condensation nuclei to form liquid droplets. Homogeneous ice nucleation of the liquid droplets can occur when the exhaust cools down through mixing with the ambient temperature, while preserving ice saturation. Small ice crystals are then formed in the jet phase within some tenths of a second (Kaercher and Yu, 2009).

The life-cycle of contrails depends on their interaction with the wake vortices behind aircraft and the ambient atmosphere (Irvine et al., 2012; Graf et al., 2012; Duda et al., 2013; Carleton et al., 2013; Schumann and Heymsfield, 2017). The ice crystals in the young contrails are captured within two counter-rotating wake vortices in the downwash behind the aircraft induced by the aircraft lift, which induce adiabatic compression, heating, and partial sublimation of the ice crystals within the primary wake (Lewellen and Lewellen, 2001; Sussmann and Gierens, 2001, Unterstrasser et al., 2008, Unterstrasser et al., 2016; Kärcher and Voigt, 2017). This primary wake may soon disappear if ambient air is subsaturated with respect to ice. In the case of supersaturation, the secondary wake becomes visible, thereby detraining ice particles from the primary wake at a higher level (Sussmann and Gierens, 1999, Kaufmann et al., 2014). Quasi-spherical ice crystals become increasingly aspherical and grow by uptake of water vapour as long as saturation with respect to ice is prevailing. In ice-saturated conditions, contrails can persist after the vortex breakdown, spread and evolve into contrail cirrus (Schumann and Heymsfield, 2017). The associated cloud cover (larger than for linear contrails alone) increases the radiative forcing of contrail cirrus (Burkhardt and Kärcher, 2011; Schumann et al., 2015).

1.2. Optical and microphysical properties of contrail phases

The assessment of the contrail radiative forcing requires, in particular, an accurate estimation of the cloud cover, the visible optical depth, the single scattering characteristics, the ice crystal effective size and habit (Yang et al., 2010; Spangenberg et al., 2013). Satellite observations

provide a comprehensive dataset to study statistically the contrail to cirrus evolution. The combined contrail tracking algorithms on the Spinning Enhanced Visible and Infrared Imager (SEVIRI) on board the Meteosat Second Generation (MSG) satellites with properties inferred by the Moderate Imaging Spectroradiometer (MODIS) on board the Terra satellite was used by Vazquez-Navarro et al., (2015) to characterize the properties of 2300 contrails. Properties included the lifetime (mean values of 1 h), the length (130 km), the optical thickness (0.34), the altitude (11.7 km) and the radiative forcing (-26 W m^{-2} for shortwave forcing over land) of these contrails.

However, detailed in situ optical and microphysical measurements are still needed to evaluate satellite products and to develop more appropriate retrieval algorithm. Discriminating contrails from natural cirrus from satellite observations remains extremely challenging. Although the optical and microphysical properties of young contrails (linear contrails) differ from natural cirrus properties, the contrail properties are highly time dependent, and persistent contrail cirrus can be embedded in thin cirrus clouds. Recent in situ measurements (Voigt et al., 2017) show that the microphysical properties of contrail cirrus can still be distinguished from natural cirrus at contrail cirrus ages up to several hours.

Most of the previous studies (Jessberger et al., 2013; Lewellen et al., 2012 ; Schumann et al., 2013) separate the contrail analysis between the two wakes phases. Primary and secondary wake properties depend strongly on atmospheric conditions and aircraft type (emission index, vortex, flight level, ambient humidity, temperature, …). In the primary wake, contrail ice crystals are quasi-spherical with values of the effective diameter (Deff) typically lower than 4 µm (Schumann et al., 2011; Gayet et al., 2012; Järvinen et al., 2016; Schumann et al., 2017b). The total number concentration of ice particles is typically larger than 1000 cm^{-3} a few seconds after contrail formation (Baumgardner and Gandrud, 1998; Petzold et al., 1997). Then, it decreases by dilution to concentrations below 200 cm^{-3} within less than a minute after contrail generation (Poellot et al., 1999; Schröder et al., 2000; Gayet et al., 2012). Gayet et al. (2012) reported mean values of ice water content of 3 mg m^{-3} and maximum extinction coefficients close to 7 km^{-1}. In agreement with these results, the recent overview on contrail studies presented in Schumann et al. (2017b) reports several microphysical properties at different stages, for different atmospheric conditions as well as comparisons with the Contrail Cirrus Prediction (CoCIP) model simulations. Their study highlights the large variability (which increases with contrail age) of contrail properties.

Several studies reported findings on the secondary wake and its evolution into contrail cirrus. Detrained from the primary wake and submitted to saturated ambient air with respect to ice, ice crystals grow rapidly, while crystal concentration decreases. Within the first minutes after formation, measurements exhibit aspherical ice crystals with effective sizes up to 6 µm, IWC between 2.5 and 10 mg m^{-3}, extinction between 2 and 3 km^{-1}, and crystal concentrations typically lower than 100 cm^{-3} (Goodman et al., 1998; Voigt et al., 2010; Kübbeler et al., 2011; Gayet et al., 2012; Jeßberger et al., 2013; Schumann et al., 2013; Poellot et al., 1999; Febvre et al., 2009; Kaufmann et al., 2014). Aged contrails can persist and evolve into contrail cirrus if the ambient air is saturated with respect to ice. After a few minutes, tracking contrails by visual navigation is challenging as contrail and contrail cirrus spread in the free troposphere. Aged contrails are often difficult to identify unambiguously (Schumann et al., 2017a).

Observations of the ice crystal shape and their growth over several tens of minutes and up to an hour illustrate that effective crystal sizes can easily exceed 20 µm with number concentrations ranging from 1 to 5 cm^{-3} (Lawson et al., 1998; Schäuble et al., 2009), extinction less than 0.5 km^{-1} (Febvre et al., 2009), and IWC up to 10 mg m^{-3} (Schröder et al., 2000; De Leon et al., 2012). At this stage, within a sustained ice-supersaturated environment, contrail microphysical properties may still differ from those of natural cirrus (Voigt et al., 2017) with concentrations of ice crystals larger than

100 µm in the order of 0.1 cm^{-3}. These crystals typically show bullet rosette type habits (Heymsfield et al., 1998; Heymsfield et al., 2010). Optical depth values can reach values of 2.3 (Atlas and Wang, 2010), corresponding to an extinction of 0.023 km^{-1}. Nevertheless, the transition from contrails to cirrus highly depends on the ambient saturation conditions. Modelling studies with typical atmospheric conditions show a temporal evolution of the optical and microphysical properties when contrails evolve to contrail cirrus clouds (Burkhardt and Kärcher, 2011; Unterstrasser et al., 2016 ; Schumann et al., 2015).

In this study, we report on a powerful alternative to classify cloud events into young contrails, aged contrails and cirrus. The method is applied to aircraft data of the CONCERT (Contrail and Cirrus Experiment) campaigns (Voigt et al., 2010, 2011, 2014). The methodology consists in implementing a Principal Component Analysis (PCA) of the angular light scattering data measured by the Polar Nephelometer. The PCA patterns are classified to yield different cluster representing specific contrail types. Corresponding optical, microphysical, and chemical properties are derived for each contrail phase (from young contrails to contrail-cirrus). This paper starts with an overview of the properties of contrails and cirrus clouds observed during two specific CONCERT flights (19 November 2008 and 16 September 2011) encompassing a series of different contrail evolution stages. These two flights contain a variety of contrail. The results from these flights can be regarded as an analytical framework which then can be compared to contrails properties of other flights.

2 CONCERT projects and data processing

2.1 CONCERT campaigns

The CONCERT-1 and CONCERT-2 campaigns took place in October/November 2008 and August/September 2011, respectively. Both campaigns deployed the DLR Falcon 20 E research aircraft from Oberpfaffenhofen, Germany, and sampled contrails and cirrus at mid-latitudes over Europe. The overall objective was to reduce uncertainties on the microphysical, chemical, and radiative properties of contrails behind aircraft of different types and to improve the evaluation of contrail's impact on climate. A few CONCERT flights were also dedicated to study emissions of Etna and Stromboli volcanos (Voigt et al., 2014; Shcherbakov et al., 2016). A few stratospheric intrusions were also observed during the flight missions. In total, 23 flights were recorded during the two measurement campaigns, wherein 12 flights were entirely focused on aircraft contrail chasing. Overall, more than 17 different aircraft exhausts plumes have been probed. CONCERT-2 campaign mainly focused on the observation of persistent contrails, and hence on the evolution of contrails to contrail cirrus.

During both CONCERT campaigns, the DLR research aircraft Falcon was equipped with a set of instruments to measure the optical and microphysical properties of cloud particles and also the trace gas composition in the UTLS (Upper Troposphere / Lower Stratosphere) region. Voigt et al. (2010) provide a detailed description of the aircraft instrumentation. We briefly introduce the instruments used in this study.

2.2 Aircraft instrumentation

The microphysical and optical particle properties of contrails and cirrus presented in this study were mainly derived from the PMS Forward Scattering Spectrometer Probe 300 (FSSP-300), the Polar Nephelometer (PN), and the PMS 2D-C hydrometeor imaging probe. The combination of these independent techniques characterizes cloud particles within a range of diameters varying from 0.5 µm to 2 mm.

180   The PN (Gayet et al., 1997) measures the angular scattering coefficients (non-normalized
181   scattering phase function) of an ensemble of water droplets or ice crystals or a mixture of those
182   particles ranging from a few micrometers to approximately 1 mm in diameter. These particles
183   intersect a collimated laser beam, at a wavelength of 804 nm, near the focal point of a parabolic
184   mirror. The light scattered at angles from 3.49° to 172.5° is reflected onto a circular array of 56
185   near-uniformly positioned photodiodes. In this study, reliable measurements were performed at 30
186   scattering angles ranging from ±15° to ±162°. Particle phase (water droplets and/or ice crystals) can
187   be assessed as well as single scattering properties such as the extinction coefficient and the
188   asymmetry coefficient with uncertainties of 25% and 4%, respectively (Gayet et al., 2002; Jourdan
189   et al., 2010).

190   Particle size distributions and corresponding microphysical and optical integrated properties
191   (IWC, Deff, N, and extinction) were derived from both FSSP-300 and 2DC measurements. The
192   FSSP-300 (Baumgardner et al., 1992) measures the intensity of forward scattered light from cloud
193   particles passing through the laser beam, with cloud particles in the diameter range 0.35-20 µm. In
194   the forward angular region (from 4° to 12°), scattering is mainly described by the particle
195   diffraction pattern and therefore depends on the refractive index, the shape, and the size of the
196   particles. The method of data processing and size calibration used during the CONCERT campaigns
197   have been presented in Gayet et al. (2012). We briefly recall that the asymmetry parameter derived
198   from the PN was used to discriminate nearly spherical particles (g ≥ 0.85) from non-spherical ones
199   (g < 0.85) at 804 nm. For spherical ice particles, Mie calculations were used to derive the size bin
200   limits and the corresponding extinction efficiency. Results were adjusted to the calibrated probe
201   response. Additionally, to minimize Mie ambiguities related to the FSSP-300 size response, 31
202   channels were rebinned to 13 channels with a diameter ranging from 0.5 µm to 18 µm (upper
203   channels 30 and 31 were excluded from the data analysis). For non-spherical particles, the size of
204   the contrail particles is expressed in terms of an equivalent surface or area diameter, i.e. the
205   diameter of a sphere that has the same area than the projected area of the measured non- spherical
206   particle image (Mishchencko et al., 1997; Schumann et al., 2011). The particles were assumed to be
207   rotationally symmetric ice ellipsoids with an aspect ratio of 0.5. Accordingly, and contrary to the
208   method used for spherical particles, 15 size bins ranging from 0.5 µm to 18 µm were defined based
209   on T-Matrix calculations following Borrmann et al., (2000).

210   The bi-dimensional optical array spectrometer probe (2DC) provides information on the
211   crystal size and shape within a nominal size range from 25 µm to 800 µm by recording cloud
212   particles shadow images with a 25 µm resolution. The method of data processing used in this study
213   is described in detail in Gayet et al. (2002) and Febvre et al. (2009). Reconstruction of truncated
214   particles has been considered for the PSD calculations and the sampling surfaces have been derived
215   according to Heymsfield and Parrish (1978). To improve the statistical significance of low particle
216   concentrations, a 5-s running mean was applied. As the sensitivity of the probe to small particles
217   decreases with airspeed (Lawson et al., 2006), particles smaller than 100 µm may not be detectable
218   at the Falcon airspeed of typically 180 m s^{-1}. This may result in larger uncertainties of up to 100%
219   in the derived microphysical parameters such as the IWC (Gayet et al., 2002 and 2004).

220   For spherical and non-spherical particles, the extinction coefficients are calculated from the
221   following equation:

$$Ext = \frac{\pi}{4} \sum_{i} \beta_{ext}^{i} N_i D_i^2 \tag{1}$$

222   where β_{ext}^{i} is the extinction efficiency (values depend on spherical or aspherical particle
223   characterization), D_i the mean diameter in channel i, and N_i the number concentration.

224 Different approaches are used to retrieve ice water content from spherical and non-spherical
225 particles (Garret et al., 2003 ; Gayet et al., 2004 ; Gayet et al., 2012). For spherical particles (gPN >
226 0.85), IWC is computed from the following equation:

$$IWC_{spherical} = \frac{\pi}{6}\rho_{ice}\sum_i N_i D_i^3 \tag{2}$$

227 with ρ_{ice} the bulk ice density (0.917 g cm^{-3}).

228 For non-spherical ice crystals (gPN < 0.85 and for particle diameters larger than 50 µm), an
229 equivalent diameter method is used (Gayet et al., 2004). For an ice crystal with an area A, the
230 particle equivalent diameter D_{equ} (in mm for eq. (3) and (4)), the equivalent mass x_{equ} (in mg), and
231 the Ice Water Content (IWC in mg m^{-3}) are defined as:
232

$$A \leq 0.049 \text{ mm}^2 \qquad\qquad D_{equ} = 0.82A^{0.48} \tag{3}$$

$$A > 0.049 \text{ mm}^2 \qquad\qquad D_{equ} = 0.56A^{0.32} \tag{4}$$

$$x_{equ} = \frac{\pi}{6}\rho_{water}D_{equ}{}^3 \tag{5}$$

$$IWC_{non-spherical} = \sum_i N_i x_{equ} \tag{6}$$

233 with ρ_{water} the bulk water density (1 g cm^{-3}).

234 These equations do not account for possible shattering of large ice crystals on the probe
235 inlets. This effect is minor in young contrails but can lead to an underestimation of large ice crystal
236 concentration (diameters higher than 100 µm) and thus an overestimation of small ice crystal
237 concentration in contrail cirrus clouds (Febvre et al., 2009).

238 Trace gas measurements were also performed. NO/NO$_y$ concentrations can be significant in
239 young tropospheric aircraft plumes. NO and NO$_y$ mixing ratio were performed using the
240 chemiluminescence technique (Schlager et al., 1997) with a time resolution of 1 s. Instruments used
241 for CONCERT campaigns are described in several studies (Jurkat et al., 2010 ; Jurkat et al., 2011 ;
242 Voigt et al., 2014 ; Jurkat et al., 2016). The accuracy (and precision) of the NO and NO$_y$
243 measurements are estimated with 7% (and 10%) and 10% (and 15%), respectively (Ziereis et al.,
244 2000).

245 Relative humidity with respect to ice (RHI) is also key parameter to understand contrail
246 formation and microphysical properties. Water vapour was measured with the chemical ionization
247 mass spectrometer AIMS-H2O during CONCERT-2 (Kaufmann et al., 2014; 2016). Hygrometers
248 using the Lyman-α technique (FISH, Zöger et al., 1999; Meyer et al., 2015), and frost point
249 hygrometers (CR-2, Heller et al., 2017) were deployed on the Falcon during CONCERT-1 and 2.

250 **3 Results**

a.

b.
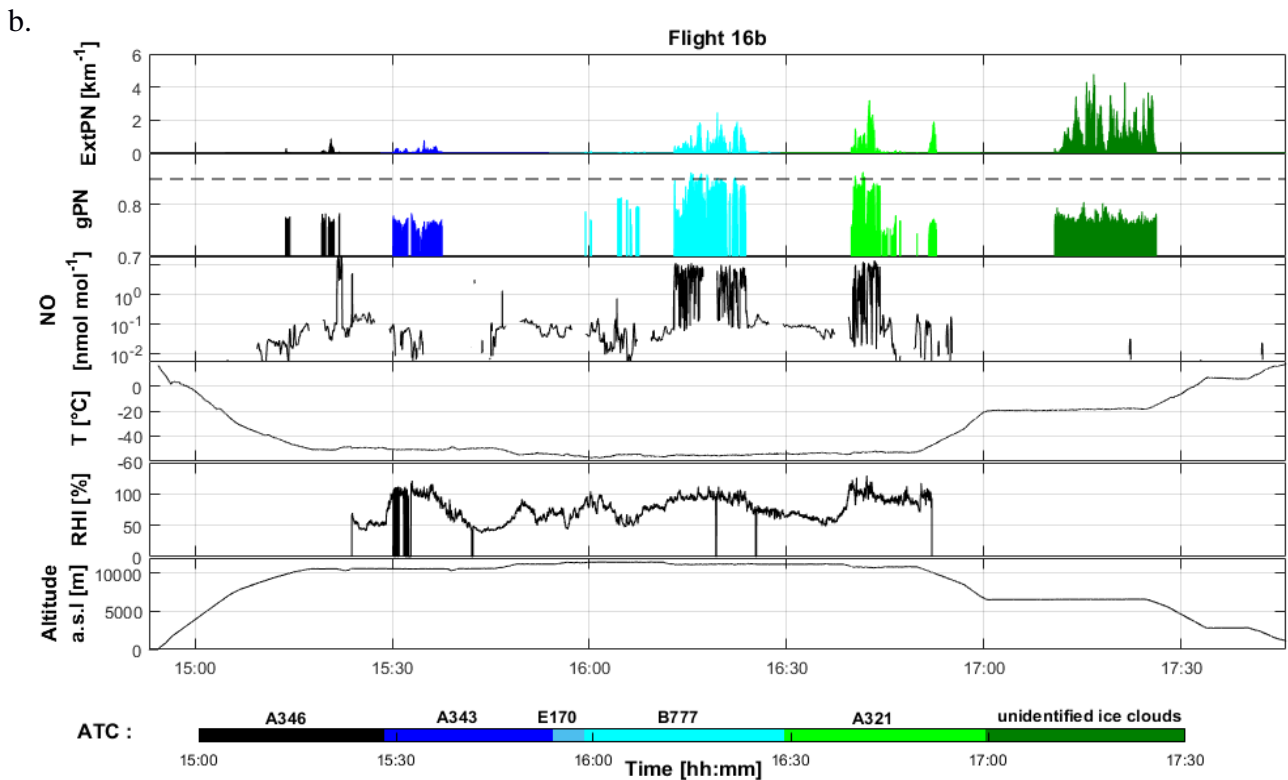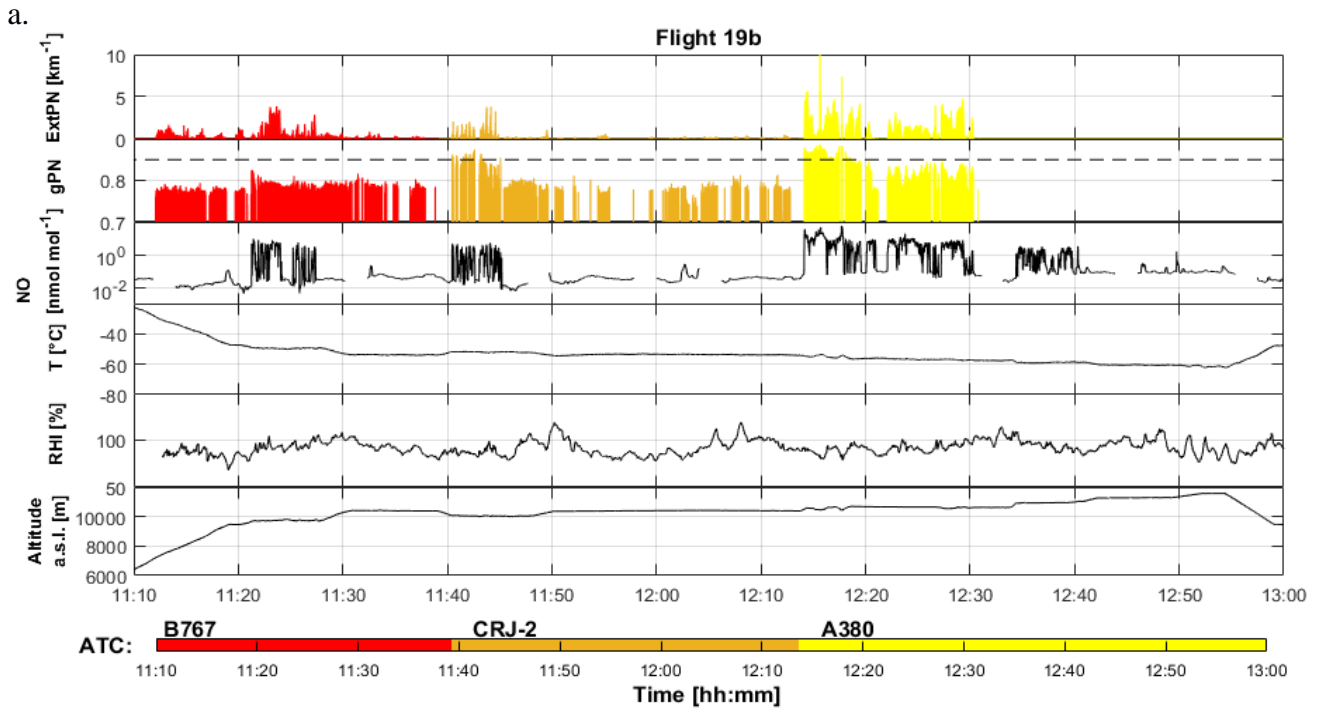
Figure 1: Time series at 1 s resolution for flights a) 19b (CONCERT 1) and b) 16b (CONCERT 2). From top to bottom: extinction coefficient (in km^{-1}) and asymmetry parameter measured by the Polar nephelometer at 804 nm (dashed line corresponds to a 0.85 value), concentration of nitric oxide (in nmol mol^{-1}) measured by chemiluminescence technique, temperature (in °C), relative humidity with respect to ice (in %), and altitude a.s.l. (in m). Temporal series are coloured according to time and aircraft chasing information from Air Traffic Control (ATC).

251   3.1 **Overview of the cloud properties sampled during the reference cases**

252   The purpose of this section is to give an overview of the contrail optical properties and more
253 interestingly to evaluate the ability of the Polar Nephelometer measurements to identify contrails.
254 Two flights, performed on 16 September 2011 during CONCERT-2 (flight 16b) and on 19
255 November 2008 during CONCERT-1 (flight 19b), respectively, were selected for their variety of
256 ice clouds sampled during these two flights. The two flights are considered as a benchmark to
257 illustrate the potential of the PCA methodology described in Sect. 3.2.

258   Figure 1 displays the time series of the extinction coefficient (ExtPN) and the asymmetry
259 parameter (gPN) at a wavelength of 804 nm, relative humidity with respect to ice (RHI), the nitric
260 oxide (NO) concentration, the temperature T and the altitude for flights 19b and 16b. RHI measured
261 with the AIMS mass spectrometer is shown for both flights. For flight 19b, RHI instrument
262 shortcomings are discussed in details in Kübbeler et al. (2011), Gayet et al. (2012), Jessberger et al.
263 (2013) and Schumann et al. (2013). For both flights, Air Traffic Control (ATC) provides
264 information on the flight tracks and on the chased aircraft (aircraft type, engine type, fuel flow,
265 weight, engine power setting). Form this information, the Falcon measurements were attributed to
266 the exhaust plume of individual aircraft with an estimated plume age. Time series are colour coded
267 according to ATC information. When no ATC information is available, the cloud segment is called
268 "unidentified ice cloud".

269   The PN extinction coefficient coupled with the asymmetry parameter seems to be a
270 reasonable proxy to detect contrails and cirrus clouds (see amongst other references, Voigt et al.,
271 2010). ExtPN values, by definition, depend on the cloud particle concentration and size. Values
272 typically beyond 0.1 km^{-1} correspond to cloud events that are well correlated to environmental
273 conditions supersaturated with respect to ice (RHI > 100%). Figure 1 shows that relatively high
274 values of extinction can be found in flights 19b and 16b that are linked to the presence of contrails
275 or ice clouds. Moreover, the temporal distributions of these values are in accordance with ATC
276 information for both flights. For instance, most of the contrails induced by commercial aircraft
277 exhaust plumes are associated with significant extinction coefficient values. The ExtPN values are
278 between 0.2 km^{-1} and 10 km^{-1} for contrails induced by A346, A340, and A380 commercial aircraft.

279   The last cloud event ("unidentified ice cloud") during flight 16b is not a contrail because it
280 is measured at temperatures significantly above the Schmidt Appleman temperature (-38°C,
281 Schumann 1996). This is an ice cloud with high extinction (> 0.5 km^{-1}) and low asymmetry values
282 (<0.75), characteristic for ice particles (Jourdan et al., 2003b, Febvre et al., 2009). Relative
283 humidity and NO mixing ratio data are not available for this cloud.

284   Most of the aircraft induced contrails are detected by the PN except for the ones stemming
285 from the E170 airplane. At 15:50 during flight 16b, ATC identified the E170 position close to the
286 Falcon flight trajectory, however the ExtPN and the NO mixing ratio remained low. Hence, the
287 E170 contrail was not probed by the Falcon. In the following we assume that only periods with
288 ExtPN values above 0.1 km^{-1} are considered as a reliable signature of contrails.

289   The absolute values of the asymmetry parameter gPN provide additional information on the
290 cloud particle shape. Indeed, gPN is a good indicator of the degree of sphericity of ice crystals
291 (Gayet et al., 2012). Ice clouds with gPN values higher or equal to 0.85 are typically composed of
292 spherical ice crystals, whereas lower values are indicative of aspherical ice particles. In a
293 supersaturated environment, crystals grow by water vapour deposition and become increasingly
294 aspherical with time. However, in very young contrails, spherical ice crystals with an asymmetry
295 coefficient around 0.85 prevail. gPN is decreasing when water vapour diffusion is generating more
296 and more aspherical crystal shapes at ice supersaturation. This can be observed for A321 chasing
297 during flight 16b where gPN is decreasing to a value of 0.75 whilst RHI remains around 100%. This

298 is not the case during B777 chasing where no gPN decrease is observed when RHI < 100%.
299 However, it is important to note that the RHI measurements during the CRJ-2 chasing events do not
300 show supersaturated conditions, whereas contrail seems persistent. Indeed, RHI measurements
301 should be discussed carefully for this campaign due to potential calibration issues.

302 A good example of the evolution of gPN is the CRJ-2 contrail observed between 11:40 and
303 11:45 during flight 19b. The sequence illustrates the potential of the gPN measurement to
304 characterize the evolution of contrail properties. The evolution of the ice crystal shape is reflected in
305 the decrease of the asymmetry parameter from 0.88 to 0.79 (uncertainties around 0.04) after only 5
306 min and down to 0.77 after 20 min. A weaker decrease of gPN values (around 0.78 ± 0.02) is then
307 observed until 12:10 corresponding to 30 min of contrail ageing. During this period, ice crystals are
308 expected to grow by water vapour diffusion. A similar decrease of gPN values has been reported by
309 Gayet et al. (2012) in the ageing contrail from an A380 aircraft, and is also visible in the present
310 study for the B767 and the A321 contrails.

311 NO concentration measurements can also be used to discriminate natural cirrus clouds from
312 clouds influenced by aircraft traffic. At the typical altitude of 10 km, NO environmental
313 concentrations are close to background values. In contrast, NO concentrations in young contrails
314 may reach several tens of nmol mol^{-1} (Voigt et al., 2010). Figure 1 shows a good correlation
315 between the expected localization of young contrails and NO concentrations. The dilution effect in
316 the upper troposphere causes an important decay of chemical concentrations. For instance, the first
317 few seconds of the A380 chasing during flight 19b are characterized by a high NO concentration
318 (up to 40 nmol mol^{-1}) followed by a fast decrease to 10 nmol mol^{-1} in the next 15 min of
319 observation time, and less than 5 nmol mol^{-1} later. NO concentrations finally decrease to
320 background levels within hours (e.g. Voigt et al., 2017). This decrease of the NO concentration is in
321 accordance with the decrease of the extinction coefficient (from 10 to 0.2 km^{-1}) and asymmetry
322 parameter (from 0.88 to 0.77). NO is mainly used as an additional contrail indicator. However,
323 during some aircraft chasing events, NO concentrations were near background levels, while mass
324 spectrometric measurements (not shown here) indicate elevated concentrations of HONO, HNO_3,
325 and SO_2 representative for contrail chemical species.

326 Flights 19b and 16b clearly show that the optical properties can be used to discriminate
327 different cloud events. A first order analysis of these parameters (supported by the ATC
328 information) can be used to roughly distinguish young contrails (mostly quasi-spherical ice crystals)
329 from aged contrails (mostly aspherical ice crystals) . This analysis is mainly qualitative and based
330 solely on a few typical parameters (Fig. 1). A more robust statistical method should be used to
331 accurately separate the different contrail phases. In the following section, scattering properties are
332 investigated more extensively to assess whether the information content of the PN scattering
333 measurements is sufficient to document changes in the contrail microphysical properties.

334 **3.2 Statistical Method**

335 In this section, we present a methodology based on a statistical analysis of the optical
336 signature of the cloud measurements. The goal is to classify the contrail properties according to the
337 aircraft origin and evolution stage. The main objective of the Principal Component Analysis (PCA)
338 is data reduction to allow a better physical interpretation of the light scattering patterns derived
339 from the Polar Nephelometer measurements (Legendre and Legendre, 1998; Jourdan et al., 2003).
340 In this study, optical properties of ice crystals in the evolving contrail environment are examined to
341 evaluate contrail evolution. This statistical analysis was already successfully applied to discriminate
342 mixed phase clouds (Jourdan et al., 2003; Jourdan et al., 2010) from liquid clouds and ice clouds,
343 and to identify porous aerosol in degassing plumes (Shcherbakov et al., 2016).

3.2.1 Reference definition

The PCA is first applied to the PN angular scattering coefficients measurements performed during flights 16b and 19b which are here considered as our reference dataset. Initially, a correlation matrix is calculated to characterize the link between each scattering angle. The PCA is designed to generate a new limited set of uncorrelated parameters, called principal components C_{lj} representative of the original data set variability.

A first implementation of the PCA is performed to detect unreliable data or out of order photodiodes. For instance, seven photodiodes presented a low signal to noise ratio and were excluded from the dataset. Flight sequences characterized by ExtPN<0.1 were also removed. Finally, flight sequences dedicated to aircraft chasing and ice cloud sampling were considered to perform a second PCA. The analysis is performed on the remaining angular scattering coefficients (4669 Angular Scattering Coefficients (ASC) representing PN measurements of flights 16b and 19b) restricted to 25 angles θ ranging from 15° to 155°. The new set of variables or coordinates, C_{lj}, can be expressed with the scalar product of the vector of reduced angular scattering coefficients $\overrightarrow{\sigma_j}(\theta)$ for the jth measurements, expressed in log scale, and the lth eigenvector $\xi_l(\theta)$ (i.e. principal component) of the total data set correlation matrix (Jourdan et al., 2010).

$$C_{lj} = (\overrightarrow{ln\sigma_j} - \langle\overrightarrow{ln\sigma}\rangle)^T . \overrightarrow{\xi_l} \tag{4}$$

where $\langle\overrightarrow{ln\sigma}\rangle$ represents the average ASC of the dataset.

The first three eigenvectors $\overrightarrow{\xi_l(\theta)}$ of the correlation matrix are displayed in Fig. 2 along with their normalized eigenvalues λ_l, representing more than 99% of the variability of the PN angular scattering coefficients (ASC).
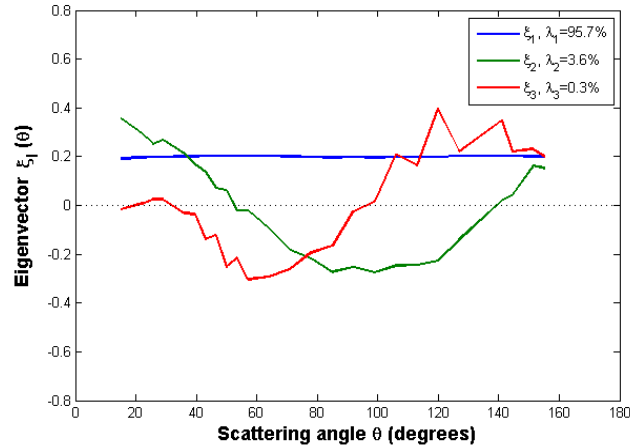
Figure 2: First three eigenvectors for the flights 16b and 19b.

The first eigenvector $\xi_1(\theta)$ is approximately constant versus scattering angle and represents 95.7% of the total variance. It means that this principal component is representative of changes of the magnitude of phase functions without any changes in their global shape. This behaviour means that 95.7% of the ASC variations are linked to changes of the cloud particle extinction. Results show a good correlation ($r^2 = 0.98$) between the first eigenvector and the extinction derived from the PN measurements (ExtPN).

370   The second eigenvector $\xi_2(\theta)$ reverses sign twice at scattering angles equal to 50° and 140°
371   with an extremum around 90°. Accordingly, 3.6% of the angular scattering variability corresponds
372   to a redistribution of scattered energy from the angular region (50°-140°) to scattering angles lower
373   than 50° and higher than 140°. Light-scattering modelling studies demonstrate that the scattering
374   behaviour in the angular region between 60° and 140° is sensitive to the particle shape and
375   thermodynamic phase (Jourdan et al., 2010). A strong linear correlation (r²=0.97) between the
376   second eigenvector and the asymmetry coefficient (gPN) at 804 nm is found.

377   The third eigenvector represents only 0.3% of the total variance. However, this eigenvector
378   provides additional information in scattering regions which are not well described by the first two
379   principal components. It has opposite signs in the angular region (30°-90°) and (90°-155°) with
380   maximum extremal values at 60° and 120°. The shape of the third eigenvector describes the
381   forward/backward hemisphere partitioning of the scattering. Baran et al. (2012), Xie et al. (2006),
382   and Xie et al. (2009) showed that the scatter pattern for angles between 120° and 160°,
383   corresponding to ice bow-like effects, is sensitive to quasi-spherical particles. Moreover, these
384   backscattering angles (θ>120°) and scattering angles around 22° and 46° (corresponding to halo
385   features) can also be linked to the particle habits and surface roughness (Xie et al., 2009, Jourdan et
386   al., 2010).

387   Each phase function (or ASC) measured by the PN can be expressed with a good accuracy
388   as a linear combination of the three principal components (Jourdan et al., 2010). The PN data are
389   projected into a new space defined by the three principal components (3D-space) instead of the 25-
390   dimensional space of ASC. The scatterplots of the C_{j3} and C_{j1} expansion coefficients versus the C_{j2}
391   coefficient are represented on Fig. 3a and b respectively. Fig. 3a illustrates the features of the ASC
392   measurements in one of the most comprehensive way. Each point corresponds to a measured phase
393   function documented over 25 angles. The variability of C_{j2} coefficients is significant with values
394   ranging from -1 to 1.5. The angular variation of the second principal component indicates that large
395   values of C_{j2} (C_{j2} > 0.75) correspond to ASC with low side scattering (60°-130°) and higher forward
396   scattering (15°-40°) and somehow higher backscattering (145-155°). This behaviour is connected to
397   an increase of the asymmetry parameter with an increase of C_{j2} values. Thus, the fraction of
398   spherical particles increases with increasing C_{j2}. In the region defined by negative values of C_{j2} the
399   density of points is relatively high. These cloud events exhibit optical properties characterized by a
400   large side scattering and low asymmetry parameter. Therefore, specific cloud sequences sharing
401   similar scattering properties can be identified based on this second principal component. Young
402   contrails characterized by quasi-spherical ice crystals have high positive values of C_{j2} while cirrus
403   clouds and contrail cirrus exhibit high negative values.
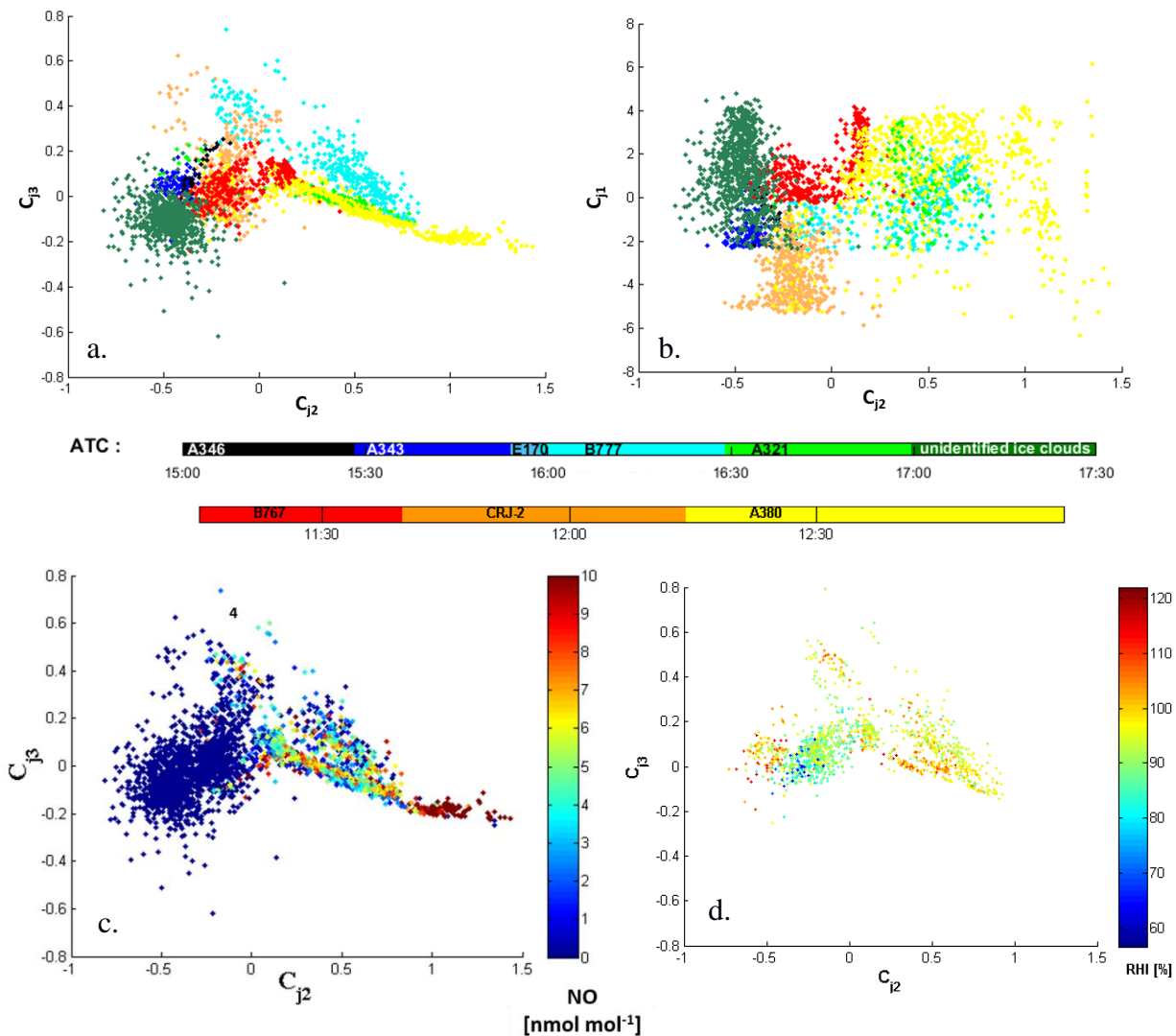
Figure 3: Expansion coefficient diagram for flights 16b and 19b: third versus second principal component for a), c) and d), and first versus second principal component for b). Data points are colour coded according to ATC information for a) and b), by NO concentration for c), and by RHI values for d).

404   In the space of the third principal component high positive values of C_{j3} imply that less
405 energy is scattering in the forward hemisphere and thus more energy is scattered in the backward
406 hemisphere. The variability of the expansion coefficients is less pronounced as ASC are distributed
407 between -0.4 and 0.6. Most of the measured ASC do not significantly differ from the average ASC
408 in the angular ranges (30°-90°) and (90°-155°). However, some specific clusters linked to scattering
409 behaviour can be identified for values of C_{j3} greater than 0.1 and lower than -0.1. These threshold
410 values also depend of the position of the ASC on the second principal component. Finally, the first
411 principal component is directly linked to the extinction coefficient. High values of C_{j1} are
412 representative of optically dense cloud sequences.

413   Figure 3c shows an increase of C_{j2} for increasing NO mixing ratio. This clearly indicates
414 that the contrails are evolving in space and/or time along the Falcon flight track. Hence, contrails
415 characterized by a low side scattering due to the presence of spherical ice crystals correspond to
416 high NO concentration. This behaviour can be a signature of young contrail properties. Elder or
417 aged contrails composed of a higher fraction of non-spherical crystals or growing more aspherically
418 are expected to exhibit an enhanced side scattering and a lower asymmetry parameter associated to

419 lower NO concentrations. RHI measurements also give relevant information on the capacity of the
420 cloud to be persistent. Thus, Fig. 3d shows higher RHI values with decreasing gPN values.

3.2.2 Clustering analyses

422 The new representation of each measurement in the space of the first three principal
423 component reveals different clusters, characteristic of specific scattering behaviour. The clustering
424 k-mean method (Seber 1984, Spath 1985) is applied to the reference dataset (fights 19b and 16b) to
425 partition the observations into k clusters to minimize the variance within each cluster (i.e. to
426 minimize the distance between each data point and the centre of the cluster it belongs to). The
427 number of cluster k is an adjustable parameter. Then in a first step, each observation is assigned to a
428 specific cluster whose mean has the least squared Euclidean distance (i.e. nearest mean). In a
429 second step, the position of each cluster is set to the mean of all data points belonging to that cluster
430 (i.e. the centroids of each of the k clusters becomes the new means). These two steps are repeated
431 until convergence is reached when the assignments no longer change.

432 Sixteen clusters were found to encompass all points of the two flights and to partition each
433 aircraft chasing identified from ATC information (Fig. 3a and 3b). For clarity and better
434 understanding of the variability of contrail properties, we choose to limit the number of clusters to
435 6. 9 of the original clusters are merged into 2 clusters (clusters 3 and 5) presenting similar NO
436 concentrations and optical properties. Four of the original clusters are combined into one new
437 cluster containing the A321 / A380 contrails (referred to as Cluster 2 hereafter). In addition, only
438 data points within the 10% of the maximum Mahalanobis distance (De Maesschalck et al., 2000) to
439 the respective cluster's centre are kept for further analysis.

440 Clusters are defined by their means (or centres), standard deviations (or widths), and cross-
441 correlations (or tilts). The Mahalanobis distance is given by the equation:

$$D_M(x)_i = \sqrt{(x - \mu_i)^T S_i^{-1} (x - \mu_i)} \tag{5}$$

442 with D_M the Mahalanobis distance between point χ and the ith cluster center, μ_i the N-dimensional
443 mean of this cluster and S_i its covariance matrix.
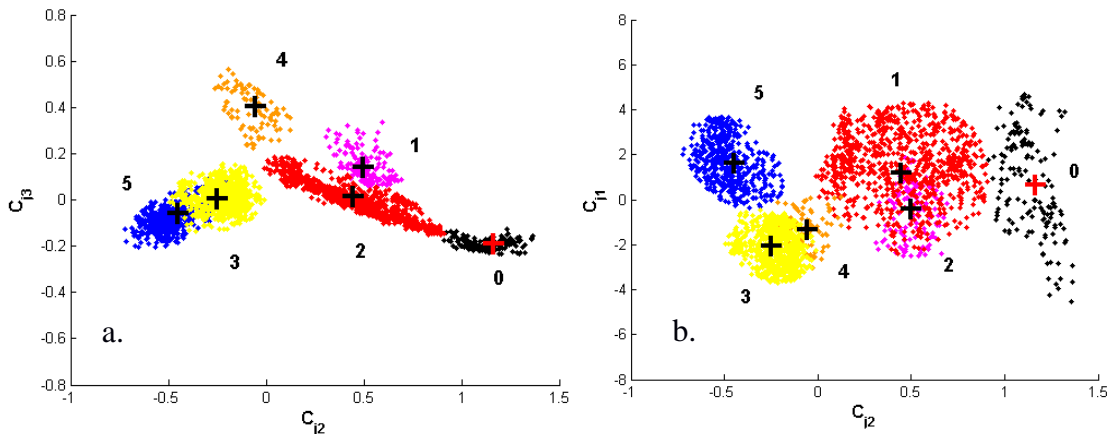
Figure 4: Clustering results of the k-mean method applied to the base (flights 16b and 19b). Third versus
second principal component for a), and first versus second principal component for b). Only data within
the 10% of the maximum Mahalanobis distance to the respective cluster's centers have been considered
for this analyse.

444 Figure 4 shows the partitioning of the dataset into the 6 new clusters (clusters 0 to 5). In the
445 following we use data from chemical tracers and optical measurements, and aircraft type
446 information to support and discuss the results of the k-means clustering method.

447 Clusters 3 and 5 are characterized by very low NO concentrations (Fig. 3c). These cloud
448 events have similar optical properties, in particular a low asymmetry parameter, high side scattering
449 behaviour, and often supersaturated ambient conditions with respect to ice. According to ATC
450 information, these clusters both contain parts of the measurements in the B767, A343, A346 and
451 CRJ-2 contrails. In addition, the unidentified ice cloud event from flight 16b is fully included in
452 cluster 5. Unpolluted natural cirrus was rarely observed during the CONCERT campaigns (Voigt et
453 al., 2010). Since we have no objective way of discriminating natural cirrus from contrail cirrus
454 region, these clouds are referred to polluted cirrus or PC, and cluster 3 to aged contrails.

455 Clusters 0, 1, 2, and 4 correspond to higher NO concentrations representative of a
456 significant aircraft exhaust influence. Contrail data for the A380 aircraft are included in clusters 0
457 and 2 while the ones corresponding to the B777 are assigned to clusters 1 and 4. Pictures from an
458 onboard camera reveal that the data in cluster 0 come mainly from the contrail in the primary wake
459 of the A380.

460 The contrail and cirrus classification based on ASC measurements appears to be consistent
461 with the independent trace gas measurements. Each cluster represented on Fig. 4 can be linked to a
462 distinct cloud event. Therefore, the combination of flights 16b and 19b can provide a relevant test-
463 bed database to discriminate contrail properties. Young contrails (spherical ice crystals) are
464 associated to clusters 0, 1 or 2, whereas aged contrails (aspherical ice crystals and high RHI values)
465 with more pristine ice are categorized in clusters 3 and 4. Table 1 summarizes the cluster definitions
466 and names used in this work.

467

Cluster number	definition	name
0	Primary Wake	**PW**
1	Young Contrail 1	**YC1**
2	Young Contrail 2	**YC2**
3	Aged Contrail 1	**AC1**
4	Aged Contrail 2	**AC2**
5	Polluted Cirrus	**PC**

Table 1: Cluster's definitions according to ATC information
and tracer measurements (NO concentrations and RHI values)

468 One should keep in mind that some points are still attributed to a particular cluster without
469 strong physical justification.

470 **3.2.3 Merging other CONCERT flights**

471 In this section, we complement the previous analysis with additional cloud optical
472 measurements performed during other CONCERT flights to increase the robustness of the method.

473   The ASC measured during other flights can be projected in the space of the principal
474 components established with flights 16b and 19b dataset. The coordinates of the data points
475 corresponding to the other flights are calculated from Eq. (4). An example of this data projection is
476 illustrated in Fig. 5 where flight 17a is represented in the C_{j2}/C_{j3} space. Each data point can be
477 attributed to one cluster previously defined by the k-mean clustering method based on flights 16b
478 and 19b dataset (black points). In other words, the ASC measured during another flight can be
479 merged (projected) into the expansion coefficient diagram displayed on Fig. 3. Data points sharing
480 similar optical properties will be close to each other on such plot. Figure 5 shows that different
481 contrail phases are observed during flight 17a. Data points are mostly grouped into cluster AC1, but
482 are also present in clusters AC2, YC2, and PW. Finally, cloud data gathered during this flight are
483 mainly categorized as young and aged contrails. We follow this methodology to project and classify
484 each additional contrail event performed during both CONCERT campaigns with minimum
485 Mahalanobis distance (see Eq. (5)).
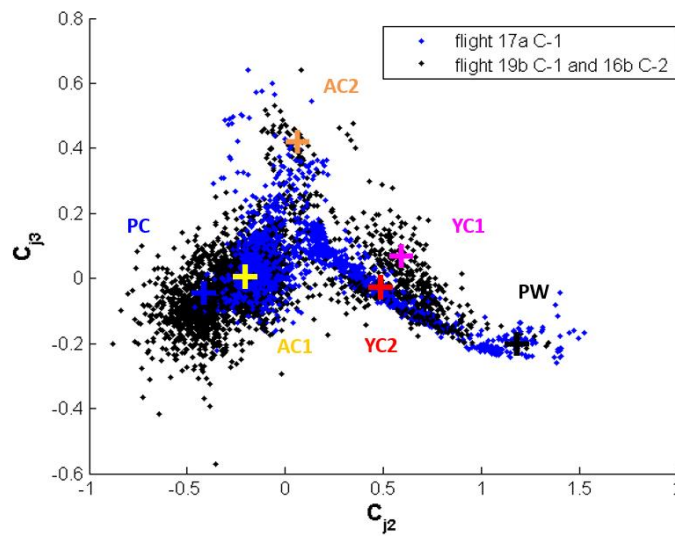
Figure 5: Example of data projection in the C_{j2}/C_{j3} space where data
from flight 17a (blue data points) are superposed on the data from
the benchmark flights 19b and 16b (black data points).

486   The assignment of the data points to the six clusters shown on the expansion diagrams is
487 summarized in Table 2. Eight flights (6 additional flights) representing 4426 ASC measurements
488 were processed. The lengths of the bars in Table 2 represent the distribution of the data points
489 within the different clusters: a) black bars correspond to the fraction of cloud events within a
490 specific flight (with extinction coefficient higher than 0.1 km^{-1}) and b) blue bars represent cases of
491 individual contrails within the flight. Data points with extinction coefficient lower than 0.1 km^{-1} are
492 not shown in the table. More than 30% of the data points are located in clusters AC1 and/or PC
493 meaning that they correspond to aged contrail and sometimes polluted cirrus. Flights clearly
494 performed in well visible contrails outside cirrus (earlier development stage and/or intensified
495 persistent elder contrails) exhibit significant fraction of data points associated to clusters PW, YC1,
496 and YC2 (young contrails) for both CONCERT-1 and CONCERT-2 campaigns. However, within
497 these flights data points are also gathered in cluster AC1 (aged contrails) and to a lesser extent in
498 cluster AC2 (mostly corresponding to measurements performed during two different B777 contrail
499 chasing events).

500   These results are in reasonable agreement with previous conclusions (this subsection) drawn
501 for the cluster definitions and associated contrail / ice cloud characteristics. Very young contrails
502 have been mostly chased during CONCERT-1 (flights 19a and 19b). Another interesting result is

related to flight 17 during CONCERT-2 (flight 17 C-2) where no aircraft information was provided by ATC. Still ATC data indicate measurements in exhaust plumes and the Falcon flew apparently in visible contrails (ExtPN > 0.1 km^{-1}) which were probably too old for ATC recognition. Our analysis shows that these data points can mainly be attributed to cluster PC and AC1. This observation suggests that significantly aged contrails have been sampled. However, crystal formation and growth processes in contrails and polluted cirrus suggest that very old contrails more and more resemble natural cirrus properties.

Day / Aitcraft			PW	YC1	YC2	AC1	AC2	PC	Number of points	Age (s)
			1st wake	young contrails		aged contrails		Polluted Cirrus		
	17a C-1	TOTAL							1435	
		A340-311							359	61 - 144
	17b C-1	TOTAL							2715	
		B737-500							310	77 - 151
		A340-642							100	82 - 139
		NC							189	-
	19a C-1	TOTAL							2152	
		A319-111							628	94 - 129
		A340-311							175	63 - 90
	19b C-1	TOTAL							1647	
		B767-300							319	77 - 107
		CRJ-2							151	80 - 95
		A380-841							677	109 - 240
	20 C-1	TOTAL							1434	
		B737-300							64	90 - 290
	16b C-2	TOTAL							1511	
		A340-600							128	100 - 132
		B777							378	120 - 160
		A321							135	70 - 95
	17 C-2	TOTAL							2904	
		NC1							498	-
		NC2							233	-
	24 C-2	TOTAL							1380	
		B777							371	112 - 178

Table 2: Classification relative to the six clusters on the Cj2/Cj3 representation of the PCA of all data points for each flight of the two CONCERT campaigns (C-1 in November 2008 and C-2 in September 2011). The legend of the bars represents the relative contribution of data points of individual contrails (blue bars) and also entire flights (black bars) to the 6 individual clusters.

ATC information on exhaust plume ages was also collected during each chasing. Some chasings were performed less than 100 s after contrail formation. This is the case for the A340 contrail during flight 19a and for the CRJ-2 contrail during flight 19b of CONCERT-1 and for the A321 contrail during flight 16b of CONCERT-2. One can notice that the contrail ages are well correlated to the chosen cluster definitions, revealing that contrail data relative to the A340 are included in cluster PW and YC2 (young contrails) for more than 90% of the data points, and nearly 63% for the CRJ-2 and 84% for the A321. According to our cluster classification, only 5% of the data points gathered during these three flights correspond to aged contrail (cluster AC1 and AC2) categories in contrast to other CONCERT-1 and CONCERT-2 flights (with more than 30% of data points associated to AC1 and AC2). Even though it is still difficult to associate contrail ages to measurement points, the "contrail age" ranges agree with the cluster definitions.

4 Evolution of contrail properties

4.1 Optical and chemical cluster properties

523   In the previous section, we showed that cloud events can be separated according to their
524   light-scattering properties. Six clusters were defined based on two flights having a significant
525   number of data points distributed in each cluster. In this section, we present the mean optical,
526   chemical, and microphysical properties for each cluster. The average properties are calculated for
527   all data points associated to the 6 individual clusters (all flights, both CONCERT campaigns).
528   Figures 6a, 6c, and 6d show the normalized frequency distributions of the asymmetry parameter
529   (gPN), the extinction coefficient (ExtPN), and NO concentrations for the six clusters, respectively.
530   Figure 6b represents the mean normalized scattering phase functions of each clusters. However, it
531   should be noted that the number of data points could differ significantly from one cluster to another
532   (from 141 measurements for Cluster YC1 to 8950 measurements for Cluster AC1).

533   The asymmetry parameter gPN statistics shown in Fig. 6a provides the most striking
534   evidence of the relationship between contrail evolution stage and optical properties. In agreement
535   with findings of Gayet et al. (2012), aged contrails (cluster AC1 and AC2) and polluted cirrus
536   (cluster PC) correspond to gPN values ranging from 0.72 to 0.80. Younger contrails (cluster YC1
537   and YC2) have values of gPN of 0.80 to 0.86. Values of the asymmetry parameter in the primary
538   wake (cluster PW) are typically above 0.86. These features are a consequence of the time evolution
539   of ice crystal shapes from quasi-spherical ice particle after exhaust to non-spherical (e.g. column,
540   needle, bullet, and bullet-rosette type crystals) as the contrail evolves. In the primary wake, the
541   pressure increases in the descending vortex. This leads to adiabatic heating and subsequent
542   sublimation of the ice crystals (Lewellen and Lewellen, 2001; Unterstrasser et al., 2016) that can
543   explain the spherical shapes of ice crystals and thus, the high values of the asymmetry coefficients.
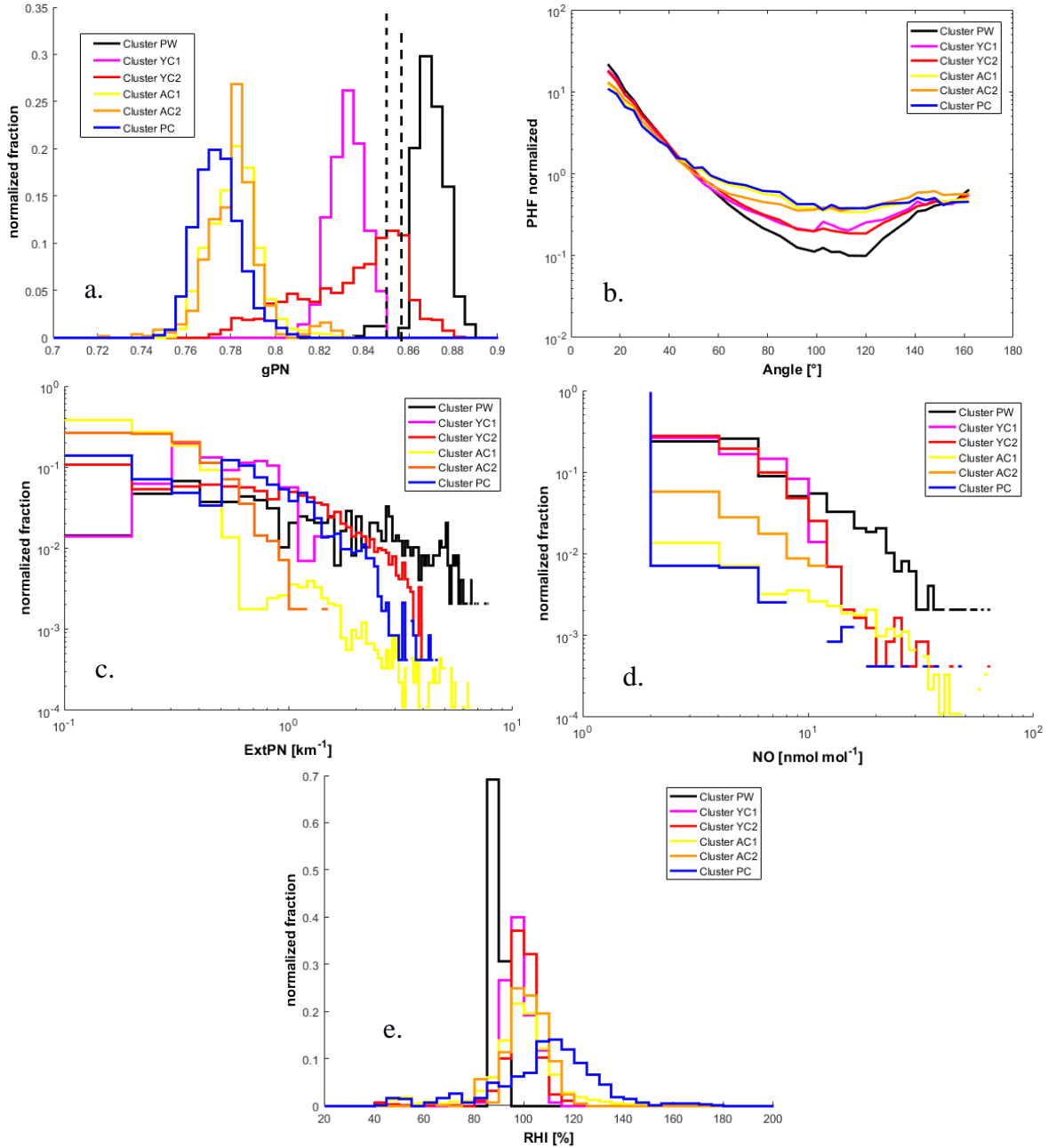
Figure 6: Normalized histograms of a) asymmetry coefficient (dashed line corresponds to a value of 0.85), b) phase function, c) extinction retrieved by Polar Nephelometer, d) NO concentration for all flights, and e) RHI conditions for CONCERT-2 flights.

544   Figure 6b shows the normalized phase functions. Primary wake phase functions (cluster
545 PW) are clearly different from the young contrail phase functions (cluster YC1 and YC2), which are
546 themselves different from aged contrails (cluster AC1 and AC2) and polluted cirrus (cluster PC)
547 phase functions. The main difference can be seen in the side scattering region (50°-140°). This
548 region is sensitive to the ice particles shapes and to the fraction of spherical ice crystals within the
549 contrails. This behaviour is as expected and agrees with the position of clusters PW, YC2 and YC1
550 on the expansion coefficient diagram (Fig. 2). Indeed, the decrease of the C_{j2} coefficient is
551 associated to a side scattering enhancement. Therefore, very young contrails are composed mainly
552 of spherical ice crystals for which the phase functions indicate a substantial scattering at forward
553 angles and much lower scattering at sideward angles. As the contrails evolve, these features smooth
554 out leading to phase functions with a featureless flat behaviour at side scattering angles. Finally, the

555 averaged normalized phase functions of aged contrails and polluted cirrus are similar to each other.
556 This also explains that they are difficult to discriminate within the PCA.

557   Figure 6c presents the extinction coefficient statistics. All the aged contrails (cluster AC1
558 and AC2) exhibit extinction coefficients lower than 2 km^{-1}. Also 80% of the sampled polluted cirrus
559 (cluster PC) show such low extinction coefficients. For younger contrails (cluster YC1 and YC2),
560 the extinction coefficients can reach 5 km^{-1}. Largest extinction coefficients are found in primary
561 wake measurements (cluster PW) with values up to 8 km^{-1}. Still, the main fraction (more than 50%
562 of data points) of young contrail data yields extinction coefficients from 0 to 1 km^{-1}.

563   Concentrations of chemical species can also be used to characterize contrail/cirrus
564 properties. The concentration depends strongly on the type of the tracked aircraft. Figure 6d shows
565 the mean concentration of nitrogen oxide NO for the six individual clusters. Young contrail NO
566 concentrations (cluster PW, YC1 and YC2) can reach values up to 10 nmol mol^{-1} (corresponding to
567 10% of measurements). For primary wake measurements (PW in black) a higher concentration can
568 be reached. Approximately 1% of the data have concentrations close to 60 nmol mol^{-1} in the
569 primary wake. In contrast, in aged contrails and in polluted cirrus (cluster AC1, AC2 and PC) NO
570 concentrations higher than 2 nmol mol^{-1} do not exceed 1% of cases. Indeed, after exhaust,
571 concentrations of nitrogen oxide NO and sulphur dioxide SO2 created by combustion reactions
572 decrease rapidly due to the dispersion in the upper troposphere and reactions with other molecules.

573   Finally, Figure 6e shows the saturation conditions with respect to ice for all clusters. The
574 median ambient relative humidity of all clusters is near 95%. Cluster AC1 and PC (yellow and blue
575 lines respectively) exhibit median RHI values close to 110% and 120% respectively. These higher
576 values are suitable for the persistence of the contrail and the formation of cirrus clouds
577 Supersaturated conditions are not reached for the measurements gathered in the primary wake
578 cluster (PW). Low humidity values may well occur in primary wakes with non-persisting contrails.

579   These results highlight that the principal component analysis, based on the ASC
580 measurements described in Sect. 3, can be used to discriminate contrail phases. Specific optical and
581 chemical properties can thus be derived for each contrail phase and can be related to their evolution.

582 **4.2 Microphysical cluster properties**

583   Microphysical properties are assessed using the combination of FSSP-300 and 2DC
584 measurements. The data cover hydrometeor diameters ranging from 0.5 µm to 800 µm, but with an
585 instrument gap in the size range from 17 µm to 50 µm. Figure 7 shows the averaged number
586 particle size distributions (PSD) for each cluster and for all flights of the study (8 flights from
587 CONCERT-1 and 2). In the instrument gap of the PSD we use linear interpolation in logarithmic
588 space. Therefore, the derived microphysical properties are to be taken with caution.

589 PSD measurements in cirrus and contrails differ significantly depending on ambient air
590 conditions, measurement methods (instrument limitation (Gayet et al., 2002), and air speed (Febvre
591 et al., 2009)). Previous studies show that a 3-h old contrail cirrus with an effective diameter close to
592 20 µm (Voigt et al., 2017) and number concentration larger than 0.1cm^{-3} (Schumann et al., 2017)
593 can be composed of ice crystals with sizes up to 100 µm (blue dashed line, contrail cirrus figure 7).
594 This differs from the PSD of the natural cirrus presented by Voigt et al. (2017) (dashed black line),
595 which has an order of magnitude lower particle number concentration. In natural cirrus at mid-
596 latitudes, ice crystals with size up to 1600 µm were observed during the ML-CIRRUS campaign
597 (dark dashed line Figure 7, Voigt et al., 2017).
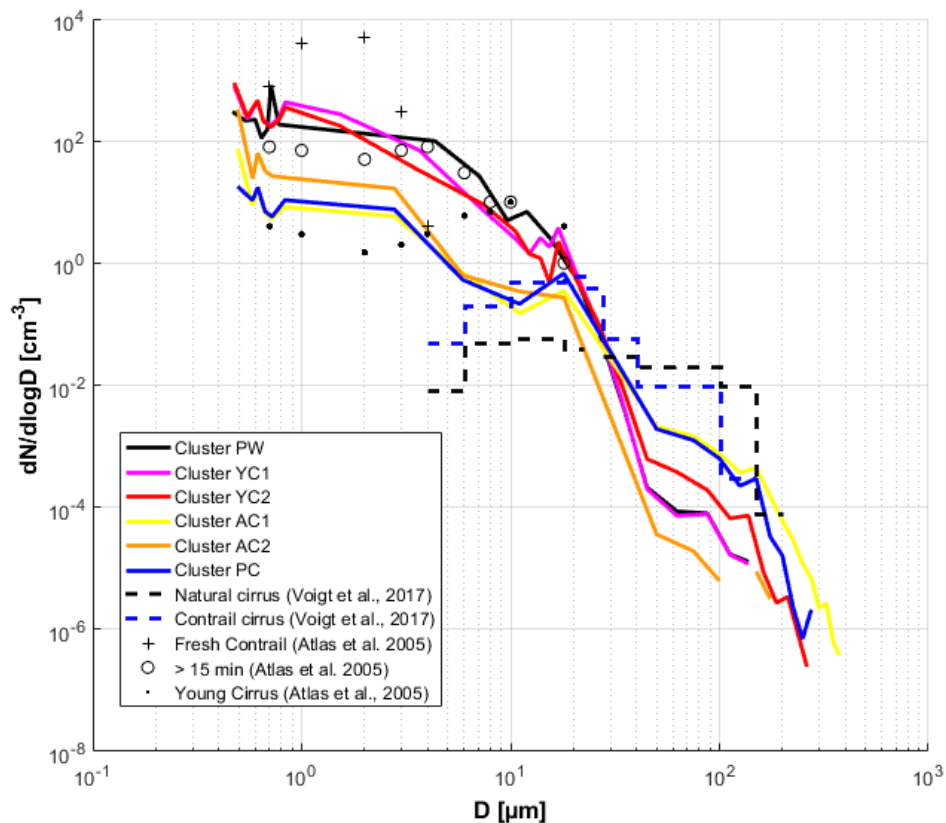
Figure 7: Number particle size distribution for each cluster including all data points of all
flights. FSSP-300 measurements from 0.5 to 17 µm and 2DC measurements from 50 µm to
800 µm. The data are linearly interpolated in logarithm space in the gap between 17 µm
and 50 µm.

598 Figure 7 shows that the mean number PSDs of each cluster are mainly consistent with the
599 cluster definition and previous studies (Atlas et al., 2009; Voigt et al., 2017). Indeed, two categories
600 of PSD can be observed. Within the FSSP-300 size range, PSD relative to old contrails (cluster
601 AC1 and AC2) and polluted cirrus (cluster PC) exhibit number concentration of small ice particles
602 one order of magnitude lower than young contrails (clusters YC1 and YC2) and primary wake
603 (cluster PW). Differences in this size range may reflect uncertainties of the FSSP-300 number
604 concentration measurements. The statistical uncertainty is close to 30% for typical concentrations of
605 5 cm^{-3} but can reach 75% for concentrations of approximately 0.5 cm^{-3} (Gayet et al., 2002).
606 However, we can still discriminate primary wake measurements (cluster PW) from secondary wake
607 measurements (clusters YC1 and YC2) in the 3 to 10 µm size range. Differences observed between
608 the PSD of PW/YC1/YC2 and AC1/AC2/PC can be explained by the production of small ice

609 crystals (from 1 to 10 µm) in fresh exhaust plumes followed by rapid dilution during subsequent
610 minutes after the exhaust.

611   Higher concentrations of ice crystals with diameters larger than 100 µm are observed for
612 polluted cirrus (cluster PC) and for well-developed contrails (cluster AC1). The average PSD of
613 AC1 cluster shows much larger ice concentrations (around 10 times) compared to YC1 cluster
614 within the 2DC size range.

615   It is important to note that shattering effects can significantly influence the PSD
616 measurements especially when particles with diameters higher than 100 µm are present. Polluted
617 cirrus or aged contrail measurements could be subject to such artefacts even though the
618 concentrations of large ice particles were low in the aged contrails and in the polluted cirrus cases
619 during these two campaigns. Shattering effects are likely to be small for the measurements in young
620 contrails.

Extinction (km^{-1})		mean	std	Median	prctile 25	prctile 75
cluster	PW	4.230	3.820	3.308	1.104	6.485
	YC1	0.720	0.410	0.680	0.351	1.026
	YC2	2.070	2.655	1.017	0.271	2.836
	AC1	0.212 (0.204)	0.465 (0.456)	0.037 (0.033)	0.008 (0.005)	0.152 (0.138)
	AC2	0.114 (0.090)	0.163 (0.149)	0.060 (0.038)	0.007 (0.003)	0.135 (0.094)
	PC	0.207 (0.197)	0.363 (0.360)	0.072 (0.062)	0.032 (0.026)	0.178 (0.160)

IWC (mg m^{-3})		mean	std	Median	prctile 25	prctile 75
cluster	PW	8.173	10.586	5.573	1.665	11.363
	YC1	0.191	0.107	0.168	0.111	0.281
	YC2	4.860	8.918	1.235	0.218	6.604
	AC1	5.707 (5.705)	25.120 (25.120)	0.124 (0.122)	0.007 (0.004)	1.126 (1.123)
	AC2	0.310 (0.304)	1.103 (1.103)	0.112 (0.093)	0.005 (0.002)	0.290 (0.285)
	PC	3.024 (3.022)	8.845 (8.845)	0.218 (0.214)	0.080 (0.079)	0.641 (0.639)

NTOTAL (cm^{-3})		mean	std	Median	prctile 25	prctile 75
cluster	PW	172.965	114.497	152.398	95.564	223.374
	YC1	409.726	205.625	405.127	230.907	603.187
	YC2	188.139	199.736	125.344	52.584	236.100
	AC1	8.148 (0.372)	24.646 (2.103)	1.688 (0.086)	0.027 (0.027)	3.311 (0.179)
	AC2	29.517 (0.427)	44.723 (1.005)	8.021 (0.128)	0.0120 (0.020)	46.762 (0.290)
	PC	6.646 (0.360)	7.237 (0.864)	4.602 (0.213)	0.110 (0.110)	8.354 (0.394)

Table 3: Optical and microphysical properties for each cluster according interpolated particle size distributions from FSSP-300 and 2DC measurements. Values in parenthesis correspond to number concentrations for sizes larger than 3 µm.

621   Table 3 presents ice water content (IWC, in mg m^{-3}) and total number concentrations of ice
622 crystals (NTOTAL, in cm^{-3}) derived from the measured PSD for each cluster. The extinction
623 coefficient (in km^{-1}) obtained from the PN measurements is also displayed. The aged contrail
624 clusters (AC1 and AC2) and the polluted cirrus cluster (PC) include some data points at
625 temperatures higher than -38°C. These values cannot be contrails and are excluded from this
626 analysis. Ice particles with diameters higher than 3 µm are considered for aged contrails and
627 polluted cirrus to exclude possible contributions from large aerosol particles, as in the earlier studies
628 of Krämer et al. (2009) and Voigt et al. (2017), and these values are shown in parenthesis. These
629 results again show that each cluster can be related to a specific contrail phase, and their properties
630 can be compared to previous studies.

In terms of cluster mean values, the microphysical and optical properties of cluster PW agree with the cloud properties expected in the primary wakes. The extinction coefficient has a mean value of 4.23 km^{-1}, IWC is close to 8 mg m^{-3}, and the number concentration yields a typical value of 173 particles cm^{-3}. These properties are in agreement with previous measurement reported by Gayet et al. (2012) with particle number concentrations close to 200 cm^{-3} for contrails less than 60 s after their formation. Their work also reports extinction coefficient around 7 km^{-1} presenting the highest values of the contrail lifetime.

Young (clusters YC1 and YC2) and aged contrails (clusters AC1 and AC2) exhibit distinctive differences in their extinction coefficients and their concentrations of ice particles. Compared to aged contrails, young contrails have higher extinction coefficients and ice number concentrations, with values larger than 0.7 km^{-1} and 170 cm^{-3}, respectively. Indeed, the averaged extinction and number concentration values of aged contrails do not exceed 0.4 km^{-1} and 30 cm^{-3} (0.5 cm^{-3} for diameters higher than 3 µm), respectively. The ice number concentrations are in agreement with previous results with values between 200 and 100 cm^{-3} for contrail ages between 60 s and 3 min, and around 5 cm^{-3} for contrail ages around 10 min (Goodman et al., 1998 ; Lawson et al., 1998 ; Schröder et al., 2000 ; Schäuble et al., 2009 ; Gayet et al., 2012 ; Voigt et al., 2017). For aged contrails, concentrations of ice particles with sizes greater than 3 µm are below 0.5 cm^{-3}, which agree with concentrations presented in other contrail studies (close to 1 cm^{-3} in Lawson et al., 1998 and Schumann et al., 2017). Also aged contrails IWC and extinction coefficients mean values lie between 0.3 mg m^{-3} and 5.7 mg m^{-3} and 0.09 and 0.2 km^{-1}, respectively. These values are only weakly sensitive to the used cut-off size (below or above 3 µm) and are in accordance with previous studies where IWC values up to 10 mg m^{-3} and extinction coefficient below 0.5 km^{-1} were measured (Schröder et al., 2000; Febvre et al., 2009; De Leon et al., 2012).

Our results also show that differences greater than 5 m mg^{-3} can be found within young contrails (YC1 and YC2) and aged contrails (AC1 and AC2) clusters. This variability could be attributed to a small number of large particles with diameter higher than 20 µm in YC1 and AC2 compared to YC2 and AC1 clusters.

Polluted cirrus properties are analysed for ice particles with size larger than 3 µm. The mean ice particle concentration of 0.36 ± 0.9 cm^{-3} is in agreement with previous cirrus studies where values are retrieved between 0.5 and 0.005 cm^{-3} (Heymsfield et al., 2016) and typical average value of 0.1 cm^{-3} was found by Voigt et al. (2017). IWC and extinction coefficients values (3.02 mg m^{-3} and 0.20 km^{-1}, respectively) are significantly higher than the value found in clean cirrus cases (0.055 mg m^{-3} and 0.023 km^{-1}, Schumann et al., 2017; Atlas and Wang, 2010), but are more consistent with median values reported from Krämer et al. (2016) and Heymsfield et al. (2016) (1.85 mg m^{-3} for temperatures between -60 and -50°C). Optical and microphysical properties of the polluted cirrus are closer to the ones obtained for aged contrails. As mentioned in section 4.1, cirrus observed during CONCERT campaigns are largely influenced by high-density air traffic over Germany and it is thus still difficult to separate aged-contrails from natural cirrus based on their scattering properties.

Conclusions

In this study, a new form of statistical analysis of contrail to cirrus evolution is presented, based on two intensive contrail measurement campaigns, CONCERT-1 and CONCERT-2. The data are used to study optical and microphysical properties of contrails during their evolution from young contrails to contrail-cirrus clouds. The combination of optical, microphysical, and chemical

airborne measurements with aircraft chasing information from ATC provides an extended view of cloud properties.

A Principal Component Analysis (PCA) methodology was applied to the measured Polar Nephelometer scattering phase function data to facilitate the discrimination of cloud properties in different contrail phases. The PCA results were derived first for two reference flights that sampled contrails and cirrus in various development stages, including the primary wake, the young secondary wake, old contrails (few minutes after formation) and polluted cirrus. For these flights, the PCA clearly demonstrates its potential to discriminate different groups of clouds, justifying the use of these two flights as a benchmark. Thereafter, the scattering phase functions measured during other CONCERT flights were projected into the space of principal components obtained from the two reference flights. Individual data points were assigned to the predefined cluster with minimum Mahalanobis distances. From the entire data set, the cloud properties in the various contrail development stages can be analysed separately.

The analysis demonstrates that the clearest separation between clusters is derived from particle shape, which impacts the scattering phase function and the derived asymmetry parameter gPN. The asymmetry parameter clearly separates young contrails (gPN of 0.72 to 0.80) from contrail/cirrus with gPN ranging from 0.80 to 0.88. Since the exact contrail age was not always known, young and aged contrails are classified also by their optical and chemical properties. The measured NO concentrations are also useful to distinguish cirrus from old contrails. However, no strictly clean cirrus has been observed during these two campaigns due to strong influence from dense air traffic over Germany.

Particle size spectra and mean ice particle number concentration, extinction and ice water content have been also determined for each cluster. The various clusters clearly show different size distributions. In good agreement with previous findings, we find that young contrails have more than a factor of ten higher number concentrations of small ice crystals (with diameters lower than 20 µm) than aged contrails. On the other hand, aged contrails and polluted cirrus contain larger ice crystals, with diameters larger than 75 µm. The optical and microphysical properties of the aged contrails are often similar to those found in ambient cirrus which may be polluted cirrus. For polluted cirrus, the agreement with previous cirrus data is better when considering only ice particles with diameter higher than 3 µm. The results show that the PCA method allows to identify and discriminate different contrail growth stages and to provide an independent method for the characterization of the evolution of contrail properties.

In agreement with Shcherbakov et al. (2016), who characterised volcanic and cirrus using optical measurements, the PCA method has been clearly shown here to be suitable for contrail studies. The additional use of microphysical and chemical measurements can be added to the PCA method in order to improve the selection of contrail phases. Different ranges of extinction or asymmetric coefficients could be also used for PCA analyses in this perspective. However, additional parameters should be carefully selected to limit the bias introduced by the limitations of the probes and the optimal selection may vary from one measurement campaign to another.

Accurate modelling of cirrus or contrails' single scattering properties is required for the interpretation of remote sensing measurements. Therefore, measurements of the optical characteristics of ice crystals in natural conditions are still needed for validation of numerical techniques and for the determination of free parameters in light scattering models. In this context, the results from the PCA could be used to develop representative parameterizations of the scattering properties and the ice crystals' shapes and sizes observed in the visible wavelength range.

721 **Acknowledgments**

722 We thank for financial support by the Helmholtz Association under contract VH-NG-309 and
723 W2/W3-60. Part of this work was funded by DFG SPP HALO 1294 contract VO1504/4-1, and by
724 the DLR project Eco2Fly in ML-CIRRUS-cirrus special issue. We thank Lufthansa, the DLR flight
725 department and the Deutsche Flugsicherung for excellent support during the campaign. The in-situ
726 data can be found in the HALO-database (https://halo-db.pa.op.dlr.de/).

727 **References**

728 Baran, A.J., Gayet, J.-F., and Shcherbakov, V.: On the interpretation of an unusual in-situ measured
729 ice crystal scattering phase function. Atmospheric Chemistry and Physics 12, 9355–9364, 2012.
730

731 Baumgardner, D., Dye, J.E., Gandrud, B.W., and Knollenberg, R.G.: Interpretation of
732 measurements made by the forward scattering spectrometer probe (FSSP-300) during the
733 Airborne Arctic Stratospheric Expedition. Journal of Geophysical Research 97, 8035–8046, 1992.
734

735 Borrmann, S., Luo, B., and Mishchenko, M.; Application of the T-Matrix Method to the
736 Measurement of Aspherical (Ellipsoidal) Particles with Forward Scattering Optical Particle
737 Counters. Journal of Aerosol Science 31, no. 7 (2000): 789–799, 2000.
738

739 Burkhardt, U., Kärcher, B., and Schumann, U.: Global modeling of the contrail and contrail cirrus
740 climate impact. Bulletin of the American Meteorological Society 91, 479–484, 2010.
741

742 Burkhardt, U. and Kärcher, B.: Global radiative forcing from contrail cirrus. Nature Climate
743 Change, 1(1), 54–58, 2011.
744

745 Carleton, A.M., Silva, A.D., Aghazarian, M.S., Bernhardt, J., Travis, D.J., and Allard, J.: Mid-
746 season climate diagnostics of jet contrail "outbreaks" and implications for eastern US sky-cover
747 trends. Climate Research, 56, 209–230, 2013.
748

749 Chen, C.-C. and Gettelman, A.: Simulated 2050 aviation radiative forcing from contrails and
750 aerosols. Atmospheric Chemistry and Physics, 16(11), 7317–7333, 2016.
751

752 Duda, D. P., Minnis, P., Khlopenkov, K., Chee, T.L., and Boeke, R.: Estimation of 2006 Northern
753 Hemisphere Contrail Coverage Using MODIS Data. Geophysical Research Letters, 40, 612-617,
754 doi:10.1002/grl.50097, 2013.
755

756 Febvre, G., Gayet, J.-F., Minikin, A., Schlager, H., Shcherbakov, V., Jourdan, O., Busen, R., Fiebig,
757 M., Kärcher, B., and Schumann, U.: On optical and microphysical characteristics of contrails and
758 cirrus. Journal of Geophysical Research: Atmospheres (1984–2012) 114, 2009.
759

760 Frömming, C., Ponater, M., Dahlmann, K., Grewe, V., Lee, D.S., and Sausen, R.: Aviation-induced
761 radiative forcing and surface temperature change in dependency of the emission altitude. Journal
762 of Geophysical Research: Atmospheres (1984–2012) 117, 2012.
763

764 Gayet, J.F., Crépel, O., Fournol, J.F., and Oshchepkov, S.: A new airborne Polar Nephelometer for
765 the measurements of optical and microphysical cloud properties. Part I: Theoretical design. In
766 Annales Geophysicae, pp. 451–459, 1997.
767

768 Gayet, J.-F., Auriol, F., Minikin, A., Ström, J., Seifert, M., Krejci, R., Petzold, A., Febvre, G., and
769   Schumann, U.: Quantitative Measurement of the Microphysical and Optical Properties of Cirrus
770   Clouds with Four Different in Situ Probes: Evidence of Small Ice Crystals. Geophysical Research
771   Letters 29, no. 24: 2230. doi:10.1029/2001GL014342, 2002.

773 Gayet, J.-F., Ovarlez J., Shcherbakov, V., Ström, J., Schumann, U., Minikin, A., Auriol, F., Petzold,
774   A., and Monier M.: Cirrus Cloud Microphysical and Optical Properties at Southern and Northern
775   Midlatitudes during the INCA Experiment. Journal of Geophysical Research: Atmospheres 109,
776   no. D20 : D20206. doi:10.1029/2004JD004803, 2004.

778 Gayet, J.-F., Shcherbakov, V., Voigt, C., Schumann, U., Schäuble, D., Jeßberger, P., Petzold, A.,
779   Minikin, A., Schlager, H., Dubovik, O., and Lapyonok, T.: The evolution of microphysical and
780   optical properties of an A380 contrail in the vortex phase. Atmospheric Chemistry and Physics.
781   12, 6629–6643, 2012.

783 Garrett, T.J., Gerber, H., Baumgardner, D.G., Twohy, C.H., and Weinstock, E.M.: Small, highly
784   reflective ice crystals in low-latitude cirrus. Geophysical Research Letters 30, 2132, 2003.

786 Gettelman, A., and Chen, C.: The climate impact of aviation aerosols. Geophysical Research
787   Letters, 40, 2785–2789, doi:10.1002/grl.50520, 2013.

789 Gierens, K. and Dilger, F.: A climatology of formation conditions for aerodynamic contrails,
790   Atmospheric Chemistry and Physics, 13, 10847-10857, doi:10.5194/acp-13-10847-2013, 2013.

792 Graf, K., Schumann, U., Mannstein, H., and Mayer, B.: Aviation induced diurnal North Atlantic
793   cirrus cover cycle. Geophysical Research Letters 39, L16804, doi:10.1029/2012GL052590, 2012.

795 Goodman, J., Pueschel, R.F., Jensen, E.J., Verma, S., Ferry, G.V., Howard, S.D., Kinne, S.A., and
796   Baumgardner, D.: Shape and size of contrails ice particles. Geophysical Research Letters 25,
797   1327–1330, 1998.

799 Heller, R., Voigt, C., Beaton, S., Dörnbrack, A., Kaufmann, S., Schlager, H., Wagner, J., Young,
800   K., and Rapp, M.: Mountain waves modulate the water vapor distribution in the UTLS,
801   Atmospheric Chemistry and Physics, doi:10.5194/acp-2017-334, Atmos. Chem. Phys., 2017.

803 Heymsfield, A.J., and Parrish, J.L.: A computational technique for increasing the effective sampling
804   volume of the PMS two-dimensional particle size spectrometer. Journal of Applied Meteorology
805   17, 1566–1572, 1978.

807 Heymsfield, A., Baumgardner, D., DeMott, P., Forster, P., Gierens, K., and Kärcher, B.: Contrail
808   Microphysics. Bulletin of the American Meteorological Society 91, 465–472, 2010.

810 Heymsfield, A. J., Krämer, M., Luebke, A., Brown, P., Cziczo, D. J., Franklin, C., Lawson, P.,
811   Lohmann, U., McFarquhar, G., Ulanowski, Z. and Van Tricht, K.: Cirrus Clouds, Meteorological
812   Monographs, 58, 2.1-2.26, doi:10.1175/AMSMONOGRAPHS-D-16-0010.1, 2016.

814 Irvine, E.A., Hoskins, B.J., and Shine, K.P.: The dependence of contrail formation on the weather
815   pattern and altitude in the North Atlantic. Geophysical Research Letters 39, L12802,
816   doi:10.1029/2012GL051909, 2012.
817

818 Järvinen, E., Schnaiter, M., Mioche, G., Jourdan, O., Shcherbakov, V.N., Costa, A., Afchine, A.,
819   Krämer, M., Heidelberg, F., Jurkat, T., Voigt, C., Schlager, H., Nichman, L., Gallagher, M.,
820   Hirst, E., Schmitt, C., Bansemer, A., Heymsfield, A., Lawson, P., Tricoli, U., Pfeilsticker, K.,
821   Vochezer, P., Möhler, O., and Leisner, T.: Quasi-spherical Ice in Convective Clouds, Journal of
822   Atmospheric Sciences, doi:10.1175/JAS-D-15-0365.1, 2016.

824 Jansen, J. and Heymsfield, A. J.: Microphysics of aerodynamic contrail formation processes,
825   Journal of Atmospheric Sciences, 72(9), 3293–3308, 2015.

827 Jeßberger, P., Voigt, C., Schumann, U., Sölch, I., Schlager, H., Kaufmann, S., Petzold, A.,
828   Schäuble, D., and Gayet, J.F.: Aircraft type influence on contrail properties, Atmospheric
829   Chemistry and Physics, 13, 11965-11984, doi:10.5194/acp-13-11965-2013, 2013.

831 Jourdan, O., Oshchepkov, S., Gayet, J.-F., Shcherbakov, V., and Isaka, H.: Statistical analysis of
832   cloud light scattering and microphysical properties obtained from airborne measurements. Journal
833   of Geophysical Research 108, 4155, 2003.

835 Jourdan, O., Mioche, G., Garrett, T.J., Schwarzenböck, A., Vidot, J., Xie, Y., Shcherbakov, V.,
836   Yang, P., and Gayet, J.-F.: Coupling of the microphysical and optical properties of an Arctic
837   nimbostratus cloud during the ASTAR 2004 experiment: Implications for light-scattering
838   modeling. Journal of Geophysical Research: Atmospheres (1984–2012) 115, 2010.

840 Jurkat, T., Voigt, C., Arnold, F., Schlager, H., Aufmhoff, H., Schmale, J., Schneider, J.,
841   Lichtenstern, M., and Dörnbrack, A.: Airborne stratospheric ITCIMS-measurements of SO_2, HCl,
842   and HNO_3 in the aged plume of volcano Kasatochi, Journal of Geophysical Research, 115,
843   D00L17, doi:10.1029/2010JD013890, 2010.

845 Jurkat, T., Voigt, C., Arnold, F., Schlager, H., Kleffmann, J., Aufmhoff, H., Schäuble, D., Schäfer,
846   M., and Schumann, U.: Measurements of HONO, NO, NOy and SO2 in aircraft exhaust plumes
847   at cruise, Geophysical Research Letters, 38, L10807, doi:10.1029/2011GL046884, 2011.

849 Jurkat, T., Kaufmann, S., Voigt, C., Schäuble, D., Jeßberger, P., and Ziereis, H.: The airborne mass
850   spectrometer AIMS – Part 2: Measurements of trace gases with stratospheric or tropospheric
851   origin in the UTLS, Atmospheric Measurement Technics, 9, 1907–1923, doi:10.5194/amt-9-
852   1907-2016, 2016.

854 Kärcher, B., and Voigt, C.: Formation of nitric acid/water ice particles in cirrus clouds, Geophysical
855   Research Letters, 33, L08806, doi:10.1029/ 2006GL025927, 2006.

857 Kärcher, B., and Voigt, C.: Susceptibility of contrail ice crystal numbers to aircraft soot particle
858   emissions, Geophysical Research Letters, 44, 8037-8046, doi:10.1002/2017GL074949, 2017.

860 Kärcher, B., and Yu, F.: Role of aircraft soot emissions in contrail formation. Geophysical Research
861   Letters, 36, L01804, doi:10.1029/2008GL036649, 2009.

863 Kaufmann, S., Voigt, C., Jeßberger, P., Jurkat, T., Schlager, H., Schwarzenboeck, A., Klingebiel,
864   M., and Thornberry, T.: In situ measurements of ice saturation in young contrails, Geophysical
865   Research Letters, 41, doi:10.1002/2013GL058276, 2014.

866

Kaufmann, S., Voigt, C., Jurkat, T., Thornberry, T., Fahey, D. W., Gao, R.-S., Schlage, R., Schäuble, D., and Zöger, M.: The airborne mass spectrometer AIMS – Part 1: AIMS-H_2O for UTLS water vapor measurements, Atmospheric Measurement Technics, 9, 939-953, doi:10.5194/amt-9-939-2016, 2016.

Krämer, M., Schiller, C., Afchine, A., Bauer, R., Gensch, I., Mangold, A., Schlicht, S., Spelten, N., Sitnikov, N. and Borrmann, S.: Ice supersaturations and cirrus cloud crystal numbers, Atmospheric Chemistry and Physics, 9(11), 3505–3522, 2009.

Krämer, M., Rolf, C., Luebke, A., Afchine, A., Spelten, N., Costa, A., Meyer, J., Zöger, M., Smith, J., Herman, R. L., Buchholz, B., Ebert, V., Baumgardner, D., Borrmann, S., Klingebiel, M., and Avallone, L.: A microphysics guide to cirrus clouds – Part 1: Cirrus types, Atmos. Chem. Phys., 16, 3463-3483, https://doi.org/10.5194/acp-16-3463-2016, 2016

Kübbeler, M., Hildebrandt, M., Meyer, J., Schiller, C., Hamburger, Th., Jurkat, T., Minikin, A., Petzold, A., Rautenhaus, M., Schlager, H., Schumann, U., Voigt, C., Spichtinger, P., Gayet, J.-F., Gourbeyre, C., and Krämer, M.: Thin and subvisible cirrus and contrails in a subsaturated environment, Atmospheric Chemistry and Physics, 11, 5853-5865, doi:10.5194/acp-11-5853-2011, 2011.

Lawson, R. Paul, Andrew J. Heymsfield, Steven M. Aulenbach, et Tara L. Jensen. « Shapes, sizes and light scattering properties of ice crystals in cirrus and a persistent contrail during SUCCESS ». Geophysical research letters 25, no 9: 1331–1334, 1998.

Lawson, R.P., O'Connor, D., Zmarzly, P., Weaver, K., Baker, B., Mo, Q., and Jonsson, H.: The 2D-S (stereo) probe: Design and preliminary tests of a new airborne, high-speed, high-resolution particle imaging probe. Journal of Atmospheric and Oceanic Technology 23, 1462–1477, 2006.

Lee, D.S., Pitari, G., Grewe, V., Gierens, K., Penner, J.E., Petzold, A., Prather, M.J., Schumann, U., Bais, A., and Berntsen, T.: Transport impacts on atmosphere and climate: Aviation. Atmospheric Environment 44, 4678–4734, 2010.

Legendre, P., and Legendre, L.: Numerical Ecology, 2nd English ed., 853 pp., Elsevier Science, New York, 1998.

De León, R.R., Krämer, M., Lee, D.S., and Thelen, J.C.: Sensitivity of radiative properties of persistent contrails to the ice water path. Atmospheric Chemistry and Physics. 12, 7893–7901, 2012.

Lewellen, D.C.: Analytic solutions for evolving size distributions of spherical crystals or droplets undergoing diffusional growth in different regimes. Journal of the Atmospheric Sciences 69, 417–434, 2012.

Lewellen, D.C., and Lewellen, W.S.: The effects of aircraft wake dynamics on contrail development. Journal of the Atmospheric Sciences 58, 390–406, 2001.

Liou, K.N., Takano, Y., Yue, Q., and Yang, P.: On the radiative forcing of contrail cirrus contaminated by black carbon. Geophysical Research Letters, 40, 778–784, doi:10.1002/grl.50110, 2013.

917 De Maesschalck, R., Jouan-Rimbaud, D., and Massart, D.L.: The Mahalanobis Distance.
918   Chemometrics and Intelligent Laboratory Systems 50, no. 1: 1–18. doi:10.1016/S0169-
919   7439(99)00047-7, 2010.

921 Meyer, J., Rolf, C., Schiller, C., Rohs, S., Spelten, N., Afchine, A., Zöger, M., Sitnikov, N.,
922   Thornberry, T. D., Rollins, A. W., Bozóki, Z., Tátrai, D., Ebert, V., Kühnreich, B., Mackrodt, P.,
923   Möhler, O., Saathoff, H., Rosenlof, K. H., and Krämer, M.: Two decades of water vapor
924   measurements with the FISH fluorescence hygrometer: a review, Atmospheric Chemistry and
925   Physics, 15, 8521–8538, doi:10.5194/acp-15-8521-2015, 2015.

927 Mishchenko, M.I., Travis, L.D., Kahn, R.A., and West, R.A.: Modeling phase functions for dustlike
928   tropospheric aerosols using a shape mixture of randomly oriented polydisperse spheroids. Journal
929   of Geophysical Research 102, 16831–16, 1997.

931 Moore, R. H., Thornhill, K. L., Weinzierl, B., Sauer, D., D'Ascoli, E., Kim, J., Lichtenstern, M.,
932   Scheibe, M., Beaton, B., Beyersdorf, A. J., Barrick, J., Bulzan, D., Corr, C. A., Crosbie, E.,
933   Jurkat, T., Martin, R., Riddick, D., Shook, M., Slover, G., Voigt, C., White, R., Winstead, E.,
934   Yasky, R., Ziemba, L. D., Brown, A., Schlager, H., and Anderson, B. E.: Biofuel blending
935   reduces particle emissions from aircraft engines at cruise conditions, Nature, 543, 411-415,
936   10.1038/nature21420, 2017.

938 Schäuble, D., Voigt, C., Kärcher, B., Stock, P., Schlager, H., Krämer, M., Schiller, C., Bauer, R.,
939   Spelten, N., De Reus, M.., Szakáll, M., Borrmann, S., Weers, U., and Peter T.: Airborne
940   measurements of the nitric acid partitioning in persistent contrails, Atmospheric Chemistry and
941   Physics, 9, 8189-8197, 2009.

943 Schlager, H., Konopka, P., Schulte, P., Schumann, U., Ziereis, H., Arnold, F., Klemm, M., Hagen,
944   D.E., Whitefield, P.D., and Ovarlez, J.: In situ observations of air traffic emission signatures in
945   the North Atlantic flight corridor. Journal of Geophysical Research 102, 10739–10, 1997.

947 Schröder, F., Kärcher, B., Duroure, C., Ström, J., Petzold, A., Gayet, J.-F., Strauss, B., Wendling,
948   P., and Borrmann, S.: On the Transition of Contrails into Cirrus Clouds. Journal of the
949   Atmospheric Sciences 57, 464–480, 2000.

951 Schumann, U.: On conditions for contrail formation from aircraft exhausts. Meteorologische
952   Zeitschrift, 5, 4–23, 1996.

954 Schumann, U., and Heymsfield, A.: On the lifecycle of individual contrails and contrail cirrus,
955   Meteorological Monographs, 58, 3.1-3.24, doi: 10.1175/AMSMONOGRAPHS-D-16-0005.1,
956   2017.

958 Schumann, U., Jeßberger, P., and Voigt, C.: Contrail ice particles in aircraft wakes and their
959   climatic importance, Geophysical Research Letters, 40, 2867-2872, doi: 10.1002/grl.50539, 2013.

961 Schumann, U., Mayer, B., Gierens, K., Unterstrasser, S., Jessberger, P., Petzold, A., Voigt, C., and
962   Gayet, J.-F.: Effective Radius of Ice Particles in Cirrus and Contrails. Journal of the Atmospheric
963   Sciences, 68, 300–321, 2011.
964

Schumann, U., Penner, J.E., Chen, Y., Zhou, C., and Graf, K.: Dehydration effects from contrails in a coupled contrail-climate model, Atmospheric Chemistry and Physics, 15, 11179-11199, doi: 10.5194/acp-15-11179-2015, 2015.

Schumann, U., Kiemle, C., Schlager, H., Weigel, R., Borrmann, S., D'Amato, F., Krämer, M., Matthey, R., Protat, A., Voigt, C., and Volk, C. M.: Long-lived contrails and convective cirrus above the tropical tropopause, Atmospheric Chemistry and Physics, 17, 2311-2346, doi:10.5194/acp-17-2311-2017, 2017a.

Schumann, U., Baumann, R., Baumgardner, D., Bedka, S. T., Duda, D. P., Freudenthaler, V., Gayet, J.-F., Heymsfield, A. J., Minnis, P., Quante, M., Raschke, E., Schlager, H., Vázquez-Navarro, M., Voigt, C. and Wang, Z.: Properties of individual contrails: a compilation of observations and some comparisons, Atmospheric Chemistry and Physics, 17(1), 403–438, doi:10.5194/acp-17-403-2017, 2017b.

Seber, G. A. F.: Multivariate analysis of variance and covariance. Multivariate observations, 433–495, 1984.

Shcherbakov, V., Jourdan, O., Voigt, C., Gayet, J.F., Chauvigne, A., Schwarzenboeck, A., Minikin, A., Klingebiel, M., Weigel, R., Borrmann, S., Jurkat, T., Kaufmann, S., Schlage, R., Gourbeyre, C., Febvre, G., Lapyonok, T., Frey, W., Molleker, S., and Weinzierl, B.: Porous Aerosol in Degassing Plumes of Mt. Etna and Mt. Stromboli. Atmospheric Chemistry Physics 16, no. 18: 11883–97. doi:10.5194/acp-16-11883-2016, 2016.

Spath, Helmuth. The Cluster Dissection and Analysis Theory FORTRAN Programs Examples. Prentice-Hall, Inc., 1985.

Sussmann, R., and Gierens, K.M.: Lidar and numerical studies on the different evolution of vortex pair and secondary wake in young contrails. Journal of Geophysical Research: Atmospheres 104, 2131–2142, 1999.

Sussmann, R., and Gierens, K.M.: Differences in early contrail evolution of two-engine versus four-engine aircraft: Lidar measurements and numerical simulations. Journal of Geophysical Research: Atmospheres 106, 4899–4911, 2001.

Vazquez-Navarro, M., Mannstein, H. and Kox, S.: Contrail life cycle and properties from 1 year of MSG/SEVIRI rapid-scan images, Atmospheric Chemistry and Physics, 15(15), 8739–8749, 2015.

Voigt C., Schlager, H., Ziereis, H., Kärcher, B., Luo, B.P., Schiller, C., Krämer, M., Popp, P.J., Irie, H., and Kondo, Y.: Nitric acid in cirrus clouds, Geophysical Research Letters, 33, L05803, doi:10.1029/2005GL025159, 2006.

Voigt, C., Schumann, U., Jurkat, T., Schäuble, D., Schlager, H., Petzold, A., Gayet, J.-F., Krämer, M., Schneider, J., Borrmann, S., Schmale, J., Jessberger, P., Hamburger, T., Lichtenstern, M., Scheibe, M., Gourbeyre, C., Meyer, J., Kübbeler, M., Frey, W., Kalesse, H., Butler, T., Lawrence, M.G., Holzäpfel. F., Arnold, F., Wendisch, M., Döpelheuer, A., Gottschaldt, K., Baumann, R., Zöger, M., Sölch, I., Rautenhaus, M., and Dörnbrack, A.: In-situ observations of young contrails - Overview and selected case studies from the CONCERT campaign, Atmospheric Chemistry and Physics, 10, 9039–9056, doi:10.5194/acp-10-9039-2010, 2010.

Voigt, C., Schumann, U., Jessberger, P., Jurkat, T., Petzold, A., Gayet, J.-F., Krämer, M., Thornberry, T., and Fahey, D.: Extinction and optical depth of contrails, Geophysical Research Letters, 38, L11806, doi:10.1029/2011GL04718, 2011.

Voigt, C., Jessberger, P., Jurkat, T., Kaufmann, S., Baumann, R., Schlager, H., Bobrowski, N., Giuffrida, G., and Salerno, G.: Evolution of CO2, SO2, HCl, and HNO3 in the Volcanic Plumes from Etna. Geophysical Research Letters, 41, 6, 2196-2203. doi:10.1002/2013GL058974, 2014.

Voigt, C., Schumann, U., Minikin, A., Abdelmonem, A., Afchine, A., Borrmann, S., Boettcher, M., Buchholz, B., Bugliaro, L., Costa, A., Curtius, J., Dollner, M., Dörnbrack, A., Dreiling, V., Ebert, V., Ehrlich, A., Fix, A., Forster, L., Frank, F., Fütterer, D., Giez, A., Graf, K., Grooß, J.-U., Groß, S., Heimerl, K., Heinold, B., Hüneke, T., Järvinen, E., Jurkat, T., Kaufmann, S., Kenntner, M., Klingebiel, M., Klimach, T., Kohl, R., Krämer, M., Krisna, T. C., Luebke, A., Mayer, B., Mertes, S., Molleker, S., Petzold, A., Pfeilsticker, K., Port, M., Rapp, M., Reutter, P., Rolf, C., Rose, D., Sauer, D., Schäfler, A., Schlage, R., Schnaiter, M., Schneider, J., Spelten, N., Spichtinger, P., Stock, P., Walser, A., Weigel, R., Weinzierl, B., Wendisch, M., Werner, F., Wernli, H., Wirth, M., Zahn, A., Ziereis, H., and Zöger, M.: ML-CIRRUS - The airborne experiment on natural cirrus and contrail cirrus with the high-altitude long-range research aircraft HALO, Bulletin of the American Meteorological Society, doi: 10.1175/BAMS-D-15-00213, 2017.

Xie, Y., Yang, P., Gao, B.-C., Kattawar, G.W., and Mishchenko, M.I.: Effect of ice crystal shape and effective size on snow bidirectional reflectance. Journal of Quantitative Spectroscopy and Radiative Transfer 100, 457–469, 2006.

Xie, Y., Yang, P., Kattawar, G.W., Minnis, P., and Hu, Y.X.: Effect of the inhomogeneity of ice crystals on retrieving ice cloud optical thickness and effective particle size. Journal of Geophysical Research: Atmospheres (1984–2012) 114, 2009.

Yang, P., Hong, G., Dessler, A.E., Ou, S.S., Liou, K.-N., and Minnis, P.: Contrails and induced cirrus: Optics and radiation. Bulletin of the American Meteorological Society 91, 473–478, 2010.

Ziereis, H., Schlager, H., Schulte, P., Velthoven, P. van, and Slemr, F.: Distributions of NO, NO x, and NO y in the upper troposphere and lower stratosphere between 28 and 61 N during POLINAT 2. Journal of Geophysical Research: Atmospheres (1984–2012) 105, 3653–3664, 2000.

Zöger, M., Afchine, A., Eicke, N., Gerhards, M-T., Klein, E., McKenna, D.S., Mörschel, U., Schmidt, U., Tan, V., Tuitjer, F., Woyke, T., and Schiller, C. : Fast in situ stratospheric hygrometers: A new family of balloon-borne and airborne Lyman alpha photofragment fluorescence hygrometers. Journal of Geophysical Research: Atmospheres, 104, 1807-1816, 1999.